NAVAL POSTGRADUATE SCHOOL

MONTEREY, CALIFORNIA

THESIS

HIGH POWER QUANTUM CASCADE LASER FOR TERAHERTZ IMAGING

by

Mun Wai Raymond Ng

March 2012

Thesis Advisor:	Gamani Karunasiri
Associate Advisor:	David C. Jenn
Second Reader:	Fabio Alves

THIS PAGE INTENTIONALLY LEFT BLANK

REPORT DOCUMENTATION PAGE			Form Approved OMB No. 0704-0188
Public reporting burden for this collection of information is estimated to average 1 hour per response, including the time for reviewing instruction, searching existing data sources, gathering and maintaining the data needed, and completing and reviewing the collection of information. Send comments regarding this burden estimate or any other aspect of this collection of information, including suggestions for reducing this burden, to Washington headquarters Services, Directorate for Information Operations and Reports, 1215 Jefferson Davis Highway, Suite 1204, Arlington, VA 22202-4302, and to the Office of Management and Budget, Paperwork Reduction Project (0704-0188) Washington DC 20503.			
1. AGENCY USE ONLY *(Leave blank)*	**2. REPORT DATE** March 2012	**3. REPORT TYPE AND DATES COVERED** Master's Thesis	
4. TITLE AND SUBTITLE High Power Quantum Cascade Laser for Terahertz Imaging		**5. FUNDING NUMBERS**	
6. AUTHOR(S) Mun Wai Raymond Ng			
7. PERFORMING ORGANIZATION NAME(S) AND ADDRESS(ES) Naval Postgraduate School Monterey, CA 93943-5000		**8. PERFORMING ORGANIZATION REPORT NUMBER**	
9. SPONSORING /MONITORING AGENCY NAME(S) AND ADDRESS(ES) N/A		**10. SPONSORING/MONITORING AGENCY REPORT NUMBER**	
11. SUPPLEMENTARY NOTES The views expressed in this thesis are those of the author and do not reflect the official policy or position of the Department of Defense or the U.S. Government. IRB Protocol Number: N/A			
12a. DISTRIBUTION / AVAILABILITY STATEMENT Approved for public release; distribution is unlimited		**12b. DISTRIBUTION CODE** A	

13. ABSTRACT (maximum 200 words)

Video rate or real-time imaging in the terahertz (THz) frequency range has become possible in the last few years with the advent of compact and high power THz sources, such as quantum cascade (QC) lasers, and the THz-sensitive vanadium oxide based microbolometer focal plane arrays. A new higher power QCL had been acquired and was characterized using FTIR spectroscopic techniques as part of this thesis. Spectral analysis revealed the center radiation frequency to be about 3.78 THz, which was close to the manufacturer's specification. Relative power analysis showed significantly higher magnitude, of at least two orders, than the previous low power QCL. Significant temperature build-up of the cryostat, where the laser was mounted, was noticed in terms of a temperature rise of about 16 Kelvins, but was not detrimental to the laser performance. Active real-time THz imaging was conducted with the laser and a 160 x 120 element microbolometer focal plane array camera, FLIR A20M. The off-axis parabolic (OAP) reflective mirrors were re-configured for the imaging experiment to ensure sufficient THz energy would be focused onto the object. This optical setup could be easily re-configured for either transmission mode, as well as reflective mode imaging experiments. A synchronization circuitry was designed to synchronously modulate the QCL pulses with the focal plane array for differential imaging. This operation would eliminate unwanted signals from the infrared background, obviating the need for dedicated spectral filters that would have significantly attenuated the THz signal as well. Preliminary experiments showed better contrast in the acquired images. Post-processing algorithms such as addition of digital gain, enhanced edges, and integration of multiple images could potentially enhance the quality of the THz images, and extend the research towards reflective and stand-off THz imaging.

14. SUBJECT TERMS Terahertz imaging, quantum cascade laser, microbolometer			**15. NUMBER OF PAGES** 69
			16. PRICE CODE
17. SECURITY CLASSIFICATION OF REPORT Unclassified	**18. SECURITY CLASSIFICATION OF THIS PAGE** Unclassified	**19. SECURITY CLASSIFICATION OF ABSTRACT** Unclassified	**20. LIMITATION OF ABSTRACT** UU

NSN 7540-01-280-5500 Standard Form 298 (Rev. 2-89)
Prescribed by ANSI Std. 239-18

THIS PAGE INTENTIONALLY LEFT BLANK

Approved for public release, distribution is unlimited

HIGH POWER QUANTUM CASCADE LASER FOR TERAHERTZ IMAGING

Mun Wai Raymond Ng
Civilian, DSO National Laboratories, Singapore
B.Eng., National University of Singapore, 2000
M.Eng., National University of Singapore, 2001

Submitted in partial fulfillment of the
requirements for the degree of

**MASTER OF SCIENCE IN
ELECTRONIC WARFARE SYSTEMS ENGINEERING**

from the

**NAVAL POSTGRADUATE SCHOOL
March 2012**

Author: Mun Wai Raymond Ng

Approved by: Gamani Karunasiri
Thesis Advisor

David C. Jenn
Associate Advisor

Fabio Alves
Second Reader

Dan C. Boger
Chair, Department of Information Sciences

THIS PAGE INTENTIONALLY LEFT BLANK

ABSTRACT

Video rate or real-time imaging in the terahertz (THz) frequency range has become possible in the last few years with the advent of compact and high power THz sources, such as quantum cascade (QC) lasers, and the THz-sensitive vanadium oxide based microbolometer focal plane arrays. A new higher power QCL had been acquired and was characterized using FTIR spectroscopic techniques as part of this thesis. Spectral analysis revealed the center radiation frequency to be about 3.78 THz, which was close to the manufacturer's specification. Relative power analysis showed significantly higher magnitude, of at least two orders, than the previous low power QCL. Significant temperature build-up of the cryostat, where the laser was mounted, was noticed in terms of a temperature rise of about 16 Kelvins, but was not detrimental to the laser performance. Active real-time THz imaging was conducted with the laser and a 160 x 120 element microbolometer focal plane array camera, FLIR A20M. The off-axis parabolic (OAP) reflective mirrors were re-configured for the imaging experiment to ensure sufficient THz energy would be focused onto the object. This optical setup could be easily re-configured for either transmission mode, as well as reflective mode imaging experiments. A synchronization circuitry was designed to synchronously modulate the QCL pulses with the focal plane array for differential imaging. This operation would eliminate unwanted signals from the infrared background, obviating the need for dedicated spectral filters that would have significantly attenuated the THz signal as well. Preliminary experiments showed better contrast in the acquired images. Post-processing algorithms such as addition of digital gain, enhanced edges, and integration of multiple images could potentially enhance the quality of the THz images, and extend the research towards reflective and stand-off THz imaging.

THIS PAGE INTENTIONALLY LEFT BLANK

TABLE OF CONTENTS

THIS PAGE INTENTIONALLY LEFT BLANK

LIST OF FIGURES

THIS PAGE INTENTIONALLY LEFT BLANK

ACKNOWLEDGMENTS

I would like to thank my sponsor, DSO National Laboratories (Singapore), for providing me with this opportunity to pursue a Master of Science degree at Naval Postgraduate School (Monterey). I would like to thank my thesis advisor, Professor Gamani Karunasiri, for his guidance and sharing of his vast experience in this area of research. His advice was most enlightening. Many thanks also go to my second reader, Dr. Fabio Alves, for his invaluable guidance in the conduct of my research work in the laboratory, as well as in the analysis of the various experimental results. I would also like to thank Professor David C. Jenn, for his guidance as my Associate Advisor, as well as Academic Associate. His advice on my thesis and academic curriculum was invaluable. I would like to acknowledge the electronic support assistance provided by Mr. Sam Barone in my laboratory work, as well as the many invaluable discussions with Mr. Brian Kearney that helped in many ways in the conduct of the experiments. Last but not least, I would like to express my greatest gratitude to my wife, Joo Ngang, for taking great care of the boys and me.

THIS PAGE INTENTIONALLY LEFT BLANK

I. INTRODUCTION

Terahertz (THz) radiation is a form of electromagnetic (EM) waves residing between the infrared and microwave regions of the EM spectrum. The THz frequency range spans from 100 GHz to 10 THz [1], corresponding to the range of 3 mm to 0.03 mm in wavelength, as shown in Figure 1. It has been traditionally termed far-infrared, and has held great promise of new applications, owing to its ability to penetrate organic materials without damage associated with ionizing radiation sources such as X-rays.

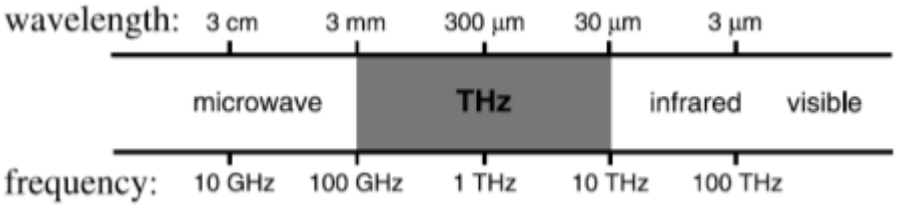

Figure 1. Electromagnetic spectrum with terahertz (THz) band highlighted. (From [1]).

However, THz applications, essentially imaging applications, have been very limited due to the strong absorption by water (H_2O) molecules in the atmosphere [2], as illustrated in Figure 2. THz applications have taken off only in the last decade with the advent of several high power THz sources, such as quantum cascade lasers (QCL) [3], [4]. Today, the list of promising applications drawing extensive research include finding defects in optically opaque materials, package inspection, and quality control. The non-ionizing property helps to extend the list of potential applications further to non-destructive testing, and spectroscopic characterization of materials. In fact, the strong water absorption characteristic is now used to distinguish between materials with varying water content [1]. Currently, the Sensor Research Laboratory (SRL) at Naval Postgraduate School (NPS) is conducting research on THz imaging using quantum cascade lasers (QCL) as illuminators and microbolometric infrared camera as sensors.

In this context, the objectives of this research include the study of the characteristics of a high power quantum cascade laser source, as well as the

synchronization of the laser with a THz-optimized microbolometric infrared camera receiver for differential imaging. The new configuration would be used to explore the feasibility of imaging various materials that are either absorptive or reflective of the THz radiation. In the long run, the high power QCL laser would be used with meta-materials that have much higher sensitivity for THz radiation to explore the feasibility of stand-off THz imaging in the reflective mode.

Chapter II provides a review of various active THz imaging techniques being researched, as well as the challenges in the development of THz sources. Chapter III describes the experimental setup and results for the characterization of a high power THz quantum cascade laser (QCL) source. Chapter IV presents the laboratory based optical setup for THz imaging, as well as the synchronization setup for the THz source and camera receiver for differential imaging. The imaging results with the quantum cascade laser source for transmissive materials are also presented.

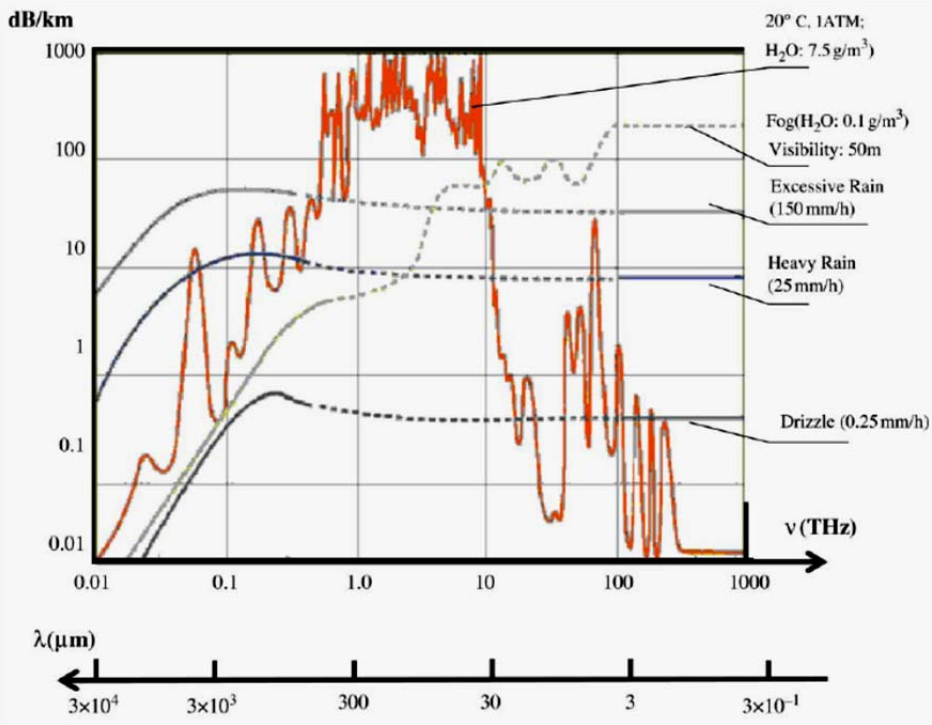

Figure 2. Plots of atmospheric attenuation versus spectral frequency at different levels of water (H_2O) content. (From [3]).

II. REVIEW OF ACTIVE TERAHERTZ IMAGING

Terahertz (THz) imaging has taken a turn for the better in the last decade with the advent of new and compact THz sources, as well as sensors with enhanced sensitivity for THz radiation. An overview on the various THz imaging techniques used, from time domain spectroscopic type imaging to real time imaging is described in detail, followed by an illustration of the challenge in the development of appropriate THz sources, as a key component of the THz imaging system. A technique to overcome strong thermal background is also presented in the last part of the chapter.

A. TERAHERTZ IMAGING TECHNIQUES

A number of THz imaging techniques have been researched in the last few decades, and some have been developed into viable applications.

1. Time Domain Spectroscopy

Terahertz time-domain spectroscopy (TDS) has been widely researched and seen tremendous progress in recent years [5]. Many interesting images, such as those shown in Figure 3, have been produced, illustrating the great promise that imaging in the terahertz spectrum could provide.

This THz TDS imaging technique exploits the measured electric field of THz radiation as a function of time, $E_{\mathrm{THz}}(t)$, to form the shape of the respective THz pulses. This coherent detection technique requires precise synchronization between the terahertz field and the gated THz detector, as shown in Figure 4. A femto-second laser is typically required to generate the THz field. Although large dynamic range is offered by coherent detection algorithms, source power is limited and the image acquisition rate is limited to scanning modes with single or linear array detectors.

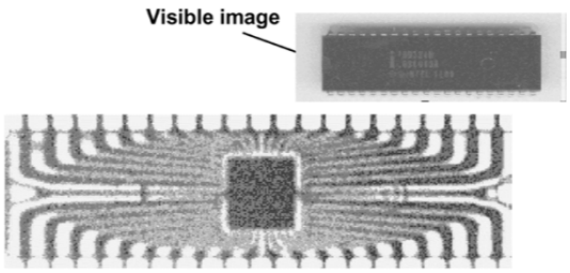

(a)

(b)

Figure 3. Time domain spectroscopy images: (a) THz TDS transmission image of a packaged semiconductor integrated circuit (IC) (From [5]), and (b) THz transmission images through a bar of chocolate of HERSHEY brand. (From [6]).

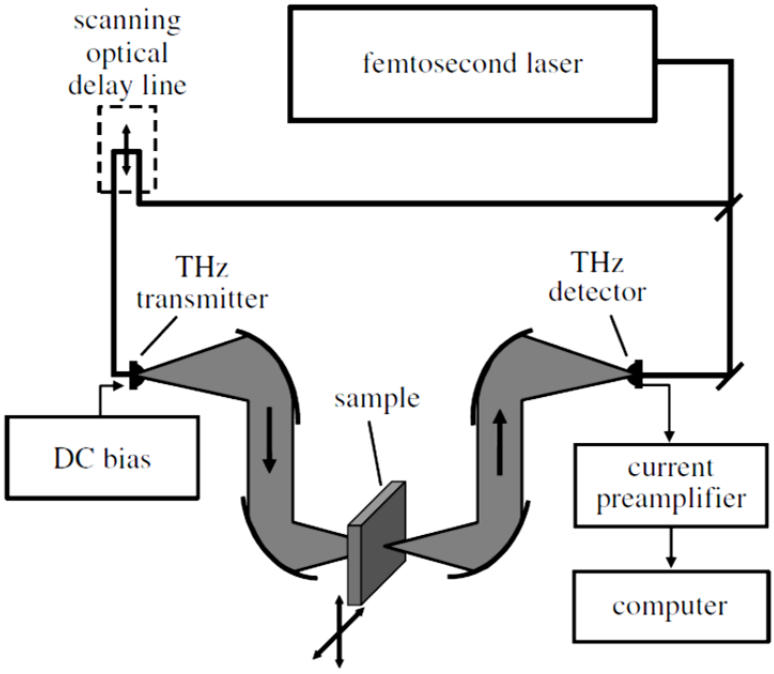

Figure 4. Schematic of a transmission mode raster scan TDS imaging system (From [1]).

2. Time of Flight Imaging

THz imaging can also be done in three dimensions, commonly known as time-of-flight (TOF) imaging, especially in a situation where the material under investigation is opaque or highly reflective to THz radiation. This technique is analogous to light detection and ranging (LIDAR) and laser detection and ranging (LADAR) techniques, where the reflection of a single transmitted pulse is collected off surfaces at different depths from the collocated transmitter and receiver. The TOF THz imaging has been extensively researched by Mittleman et al. [7] and demonstrated as shown in Figure 5 with a typical floppy disk. The two-dimensional intensity image of the floppy disk is presented in (a), while the third dimension (i.e., depth profile) along the dotted line in the top image in (b) is presented in the bottom plot in (b). The top and bottom layers are apparent from the plot, as well as the highly reflective metal hub, as indicated.

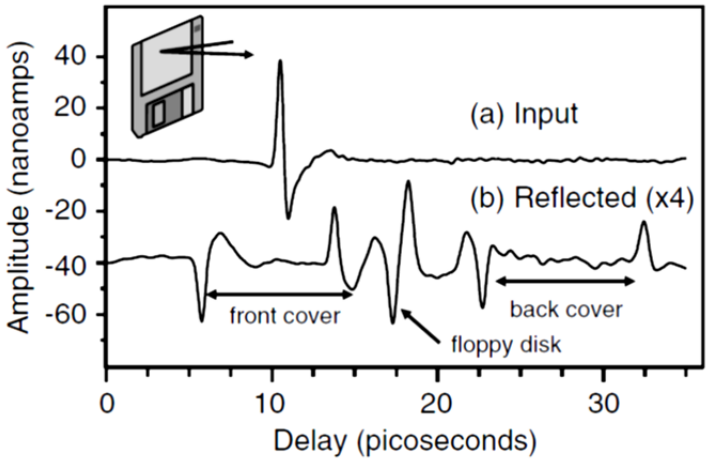

(a)

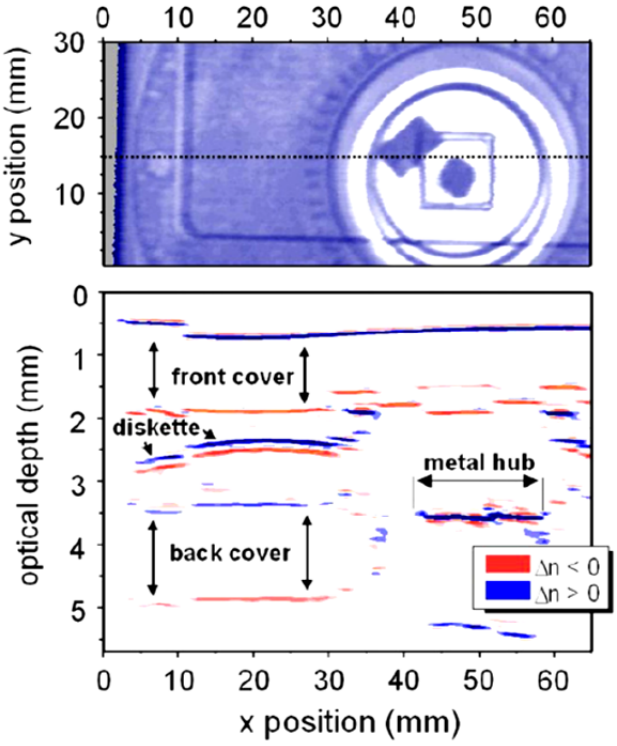

(b)

Figure 5. Time-of-flight (TOF) images: (a) Measured return signals of a single transmitted THz pulse reflected off the multiple interfaces of a conventional 3.5" floppy disk, and (b) THz reflective image of the floppy disk (top), and depth profile image (along the dotted line) of the floppy disk (bottom). (From [7]).

Two primary challenges are the normally-unknown reflectivity of the material, and the depth resolution that can be achieved. A complex reflection coefficient would distort the phase changes along the propagation direction, thus making it difficult to distinguish the different layers. Two closely spaced reflecting interfaces can only be distinguished if the returned THz signals do not overlap significantly. This depth resolution is given by half the coherence length of the radiation, i.e., $\frac{1}{2}L_c = \frac{1}{2}\frac{c}{\Delta\omega}$, where $\Delta\omega$ is the spectral width and c is the speed of light in the intervening medium. The factor of half (1/2) arises from the fact that the signal must transit through the intervening medium twice.

This TOF THz imaging technique has also been extended to tomographic imaging, where more transmitters and receivers are synchronized to image the object at various points of view, and the final three-dimensional image is a complex integration of all the range images.

3. Video Rate or Real Time THz Imaging

The more desirable technique of THz imaging is to acquire the full two-dimensional intensity image in each scan rather than acquiring image data pixel by pixel as in the aforementioned techniques. Video rate or real-time imaging has been made possible in recent years with the advent of new high power THZ sources such as QCLs, as well as imagers with enhanced THz sensitivity.

Lee et al. [8], [9] have demonstrated real time THz imaging with a high power QCL, and have extended the research to stand-off (more than a few meters) imaging at up to 25 meters [10]. Similarly, Behnken et al. [11], [12], [13] have demonstrated real-time THz imaging with both a 2.8 THz QCL and a 3.6 THz QCL, together with a microbolometric infrared camera at NPS. The laboratory setup used by Lee et al. [8], as shown in Figure 6, included the QCL with its divergent output collimated by an f/1 (50 mm diameter) off axis parabolic (OAP) mirror. A second OAP mirror (f/2) was used to capture the THz radiation and refocusing it to back-illuminate the object (an envelope), while an f/1, 25 mm-diameter, Si lens brought the illuminated object into focus at the focal plane array. The focal plane array is a commercial 320 x 240 pixel uncooled

vanadium oxide based microbolometer camera (Model SCC500 from BAE Systems). The stand-off experimental setup by Lee et al. [10], as shown in Figure 7, involved the same laser source with collimating OAP, followed by a precisely folded optical path of about 24 meters to a large object (being back-illuminated again), before being focused by a spherical mirror, and collected by an f/3 Si meniscus lens onto the same camera. A smaller object could also be imaged in the stand-off setup with the used of the f/2 OAP after the spherical mirror.

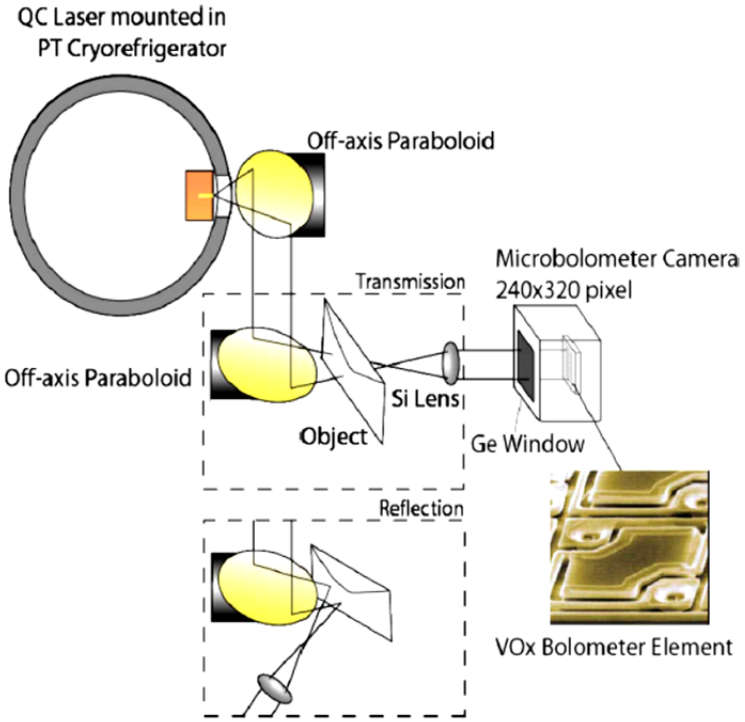

Figure 6. Real time imaging setup: laboratory based THz imaging setup in transmission and reflection configurations. (From [8]).

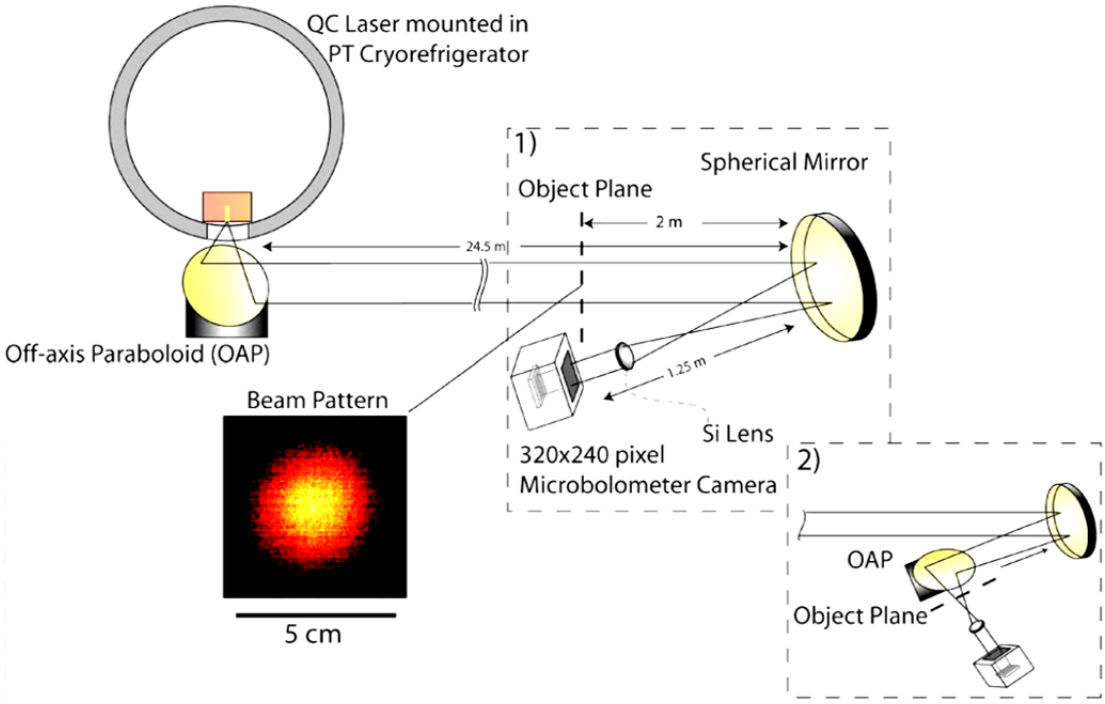

Figure 7. Stand-off THz imaging setup in transmission configuration. (From [10]).

B. TERAHERTZ SOURCES

THz radiating source has been the most challenging component in active THz imaging system. From the energy generation perspective, for an optical style source, such as a solid-state semiconductor source, THz photon energy levels (E_{ph}) will be in the range of a few meV, as illustrated by Equation (2.1), where h is the Planck's constant. These energy levels are comparable in magnitude to that of lattice phonons (E_{th}), as illustrated by Equation (2.2), where k is Stefan-Boltzmann constant. As such, cryogenic cooling would be necessary to mitigate the problem.

$$E_{ph}(f = 1\,\text{THz}) = hf \approx 4\,\text{meV} \tag{2.1}$$

$$E_{th}(T = 300\,\text{K}) = kT \approx 26\,\text{meV} \tag{2.2}$$

In the last decade, the development of THz sources has focused much on the enhancement of output power, as well as the shrinking of the component size [2]. The

average output power has increased by several orders of magnitude, as illustrated in Figure 8, with the advent of laser based THz sources, such as the quantum cascade (QC) laser [3], [14–17] and p-Germanium (pGe) laser [2].

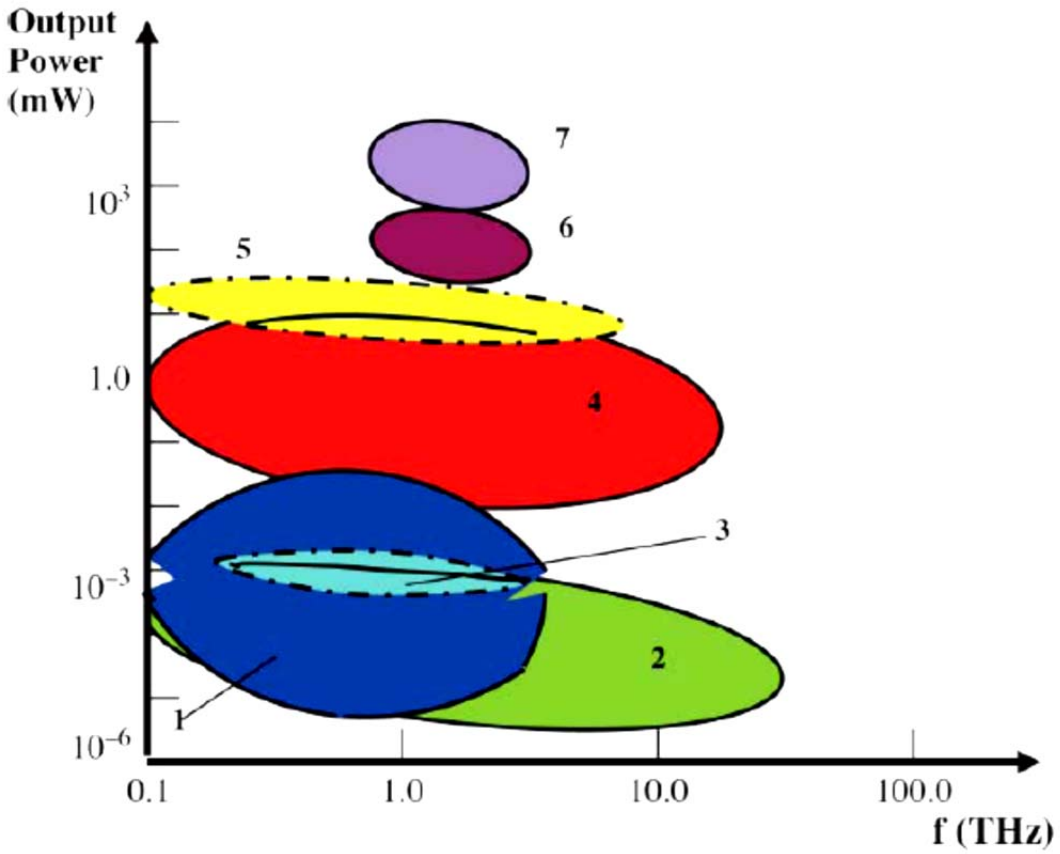

Figure 8. Output average power ranges of various terahertz sources: 1 – Photo-Conductive Antenna (PCA); 2 – Optical Rectification (OR); 3 – CO_2 Laser Frequency Mixing (CO2); 4 – Difference Frequency Generation (DFG); 5 – Optically Pumped Laser (OPL); 6 – Quantum Cascade Laser (QCL); 7 – p-Germanium Laser (pGe). (From [2]).

C. DIFFERENTIAL IMAGING

Background noise is inevitable in visible imaging applications, and can be excessive in the use of thermal imager for THz sensing, as the background infrared signature could overwhelm the already weak THz signal from the object. For real-time THz imaging with an uncooled microbolometer focal plane array camera, which is also sensitive over the long-wave infrared (LWIR) spectrum, it is inevitable that background LWIR radiation would penetrate into the focal plane array and contribute significantly to the already weak THz image.

Lee et al. [8] have implemented real-time THz imaging with a slower rate sampling sequence. In it, a background frame with minimal THz signal was acquired, and subtracted from the image frame with the THz laser illumination signal. This background subtraction or differential imaging technique has the dual purpose of removing fixed pattern noise, as well as alleviating the fluctuating infrared background without the use of a high-pass filter, which would have attenuated the THz signal significantly.

Thermal time constant is the key parameter in determining the sampling time. This time constant is the time taken for a given pixel in a thermal imager to change its temperature with respect to the incident flux intensity. Lee et al. [8] have quantified the thermal time constant for their microbolometer camera to be about 13 ms, as shown in Figure 9, for both rise and fall times. Hence, THz laser pulsing was reduced to 20 Hz, which is one-third of the normal image acquisition rate or video rate of 60 Hz. The third frame with minimum THz radiation energy was used to subtract from the first frame with full THz illumination.

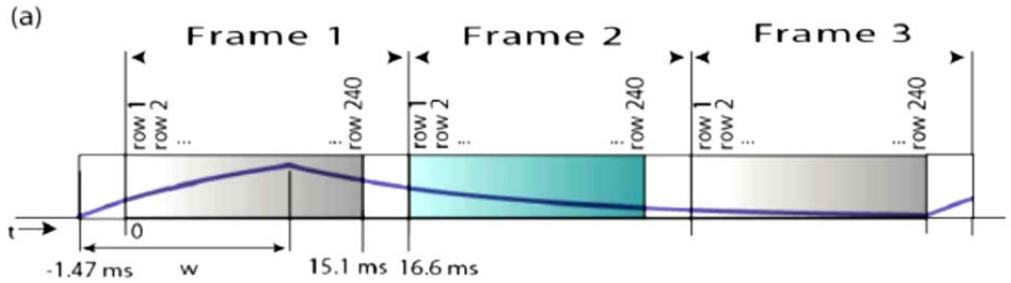

Figure 9. Signal level in the same pixel over three frame periods. Signal data from frame 3 is subtracted from that for frame 1 to remove the infrared background. (From [8]).

II. QUANTUM CASCADE LASER CHARACTERIZATION

This chapter starts with the detailed description of the experimental setup for quantifying the spectral, power, as well as the temporal performance of high power quantum-cascade (QC) lasers. The characteristics of a Fourier Transform Infra-Red (FTIR) spectrometer used for the quantification experiments are reviewed. The data collection procedures are also outlined. The results are presented with the detailed analysis in the later sections of the chapter.

A. EXPERIMENTAL SETUP

1. FTIR Spectrometer

The FTIR spectrometer used in this experiment is Nexus 870 from Thermo Nicolet. It is a Michelson interferometer with THz-reflective beam splitter and a Deuterated Triglycine Sulfate (DTGS) sensor for sensing 1.5 THz to 18 THz. The window for the external port has been replaced with a polyethylene sheet, which is almost transparent to THz radiation.

A dedicated software program, OMNIC, has been used to control the FTIR in performing the spectroscopic measurements. For all the spectral and power measurements, the speed of the scanning mirror has been set to 0.1581 m/s, while the gain and aperture have been set to the minimum setting of 1. These settings were found to be necessary due to the high power output of the QCL under test. Slower scanning speed and higher gain and aperture settings would inevitably saturate the detector. The spectral scan resolution has been set to 1 cm^{-1} to ensure precise determination of the spectral peaks in the current QCL.

2. Laser and Cryostat Assembly

The QCL was mounted onto a copper heat-sink, as shown in Figure 10, to assure conductive heat transfer away from the QCL during operation.

There are three working QCLs on the laser assembly labeled C, K and J, as illustrated in Figure 11. Laser C and Laser J have the similar width of 100 μm, while

Laser K has doubled the width. The electrical resistance of each laser (C, K and J) was measured to be 5 Ω, 3.5 Ω, and 5.1 Ω, respectively. It is expected that the Laser C and Laser J will have very similar output power performance, while that of Laser K should be significantly higher.

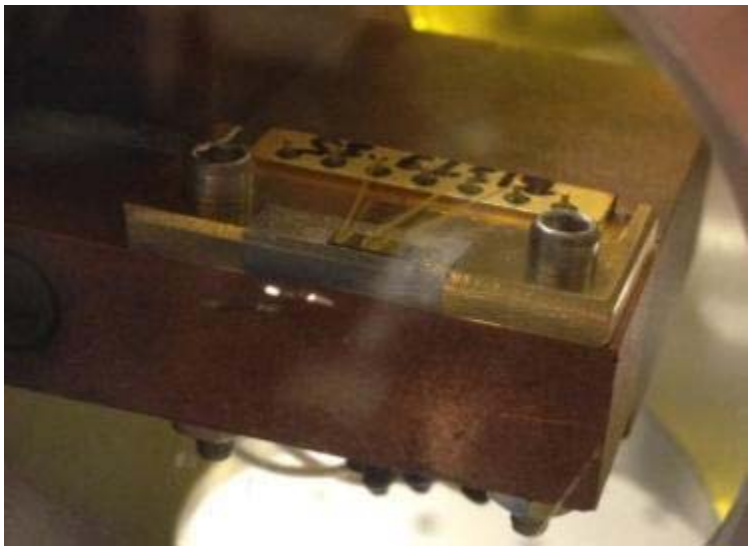

Figure 10. QCL assembly with copper heat-sink.

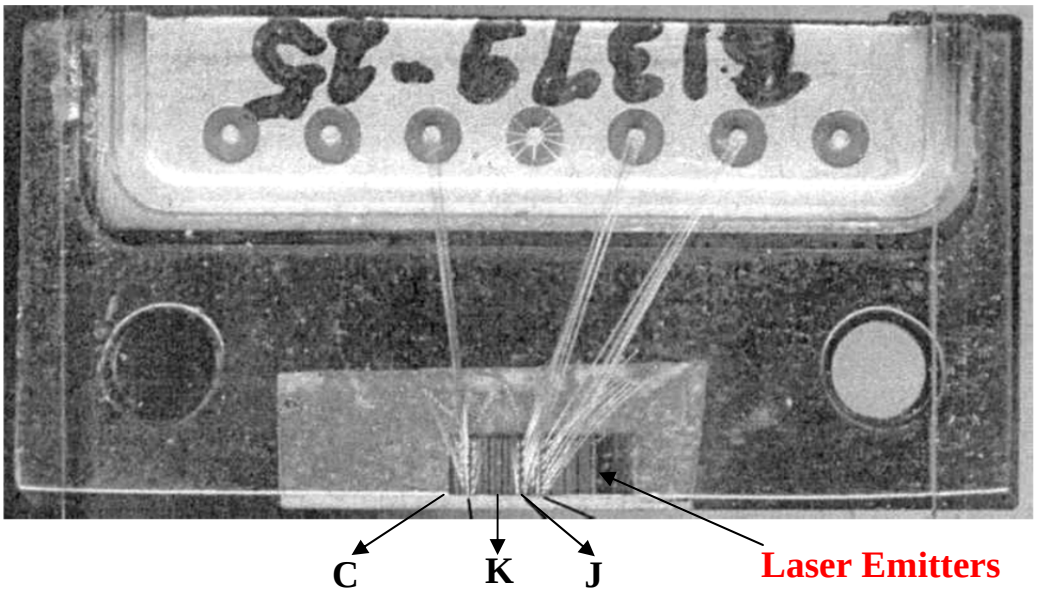

Figure 11. QCL emitters (labeled C, K and J) on the laser assembly.

The laser assembly with heat-sink was placed in the cryostat enclosure, with the emitters facing the THz-transparent Tsurupica window, as shown in Figure 12. The distance between the laser emitters and the window was measured to be approximately 20 mm, which was optimized to allow most of the divergent laser beam to transmit through the window, and be collected by the focusing optics.

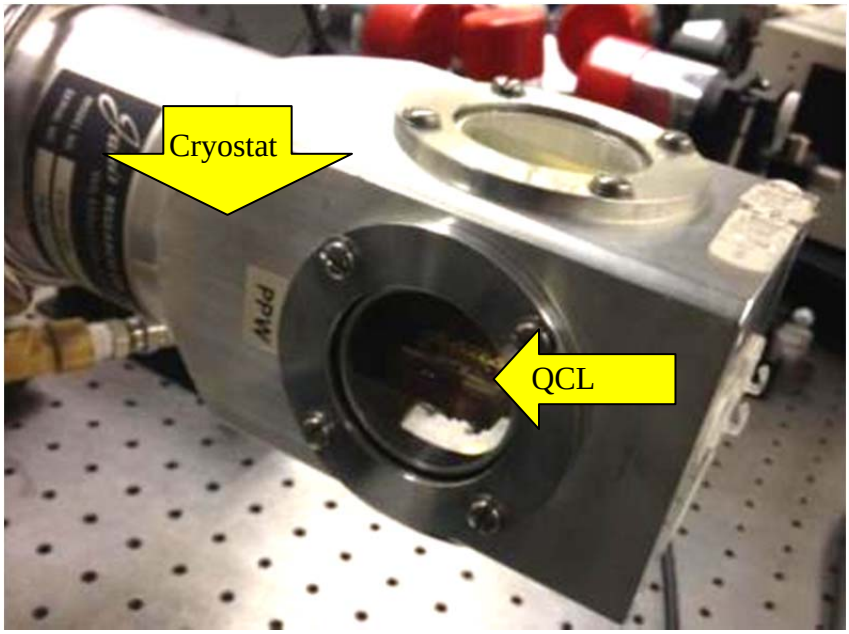

Figure 12. QCL and cryostat assembly.

3. Focusing Optics

The alignment of the QCL beam into the FTIR spectrometer was done in two steps. The first step involved the use of a front-face gold-plated 90-degree f/1 off axis parabolic (OAP) mirror, with exit aperture and focal length of 50 mm to collimate the QCL. The OAP mirror was placed right at the laser exit window. The exact position of the OAP mirror was determined using a highly collimated HeNe laser beam. The commercial HeNe laser has a typical divergence of about 1 mrad, and an exit beam diameter of about 1 mm. Coupling the HeNe laser with a 20 times beam expander increases the beam diameter to about 20 mm, but with improved collimation to a divergence of only 50 μrad.

The HeNe laser was placed on the optical axis of the OAP mirror, such that a focused beam spot would be formed at the focal point of the mirror. The mirror was first translated in x-direction to 'move' the focused beam spot onto the laser emitter surface, as shown in Figure 13. The OAP mirror was then translated along the y-direction to "move" the focused beam spot onto the desired laser emitter, such as Laser C. This set of procedures ensures that the QCL will be collimated precisely with the OAP mirror.

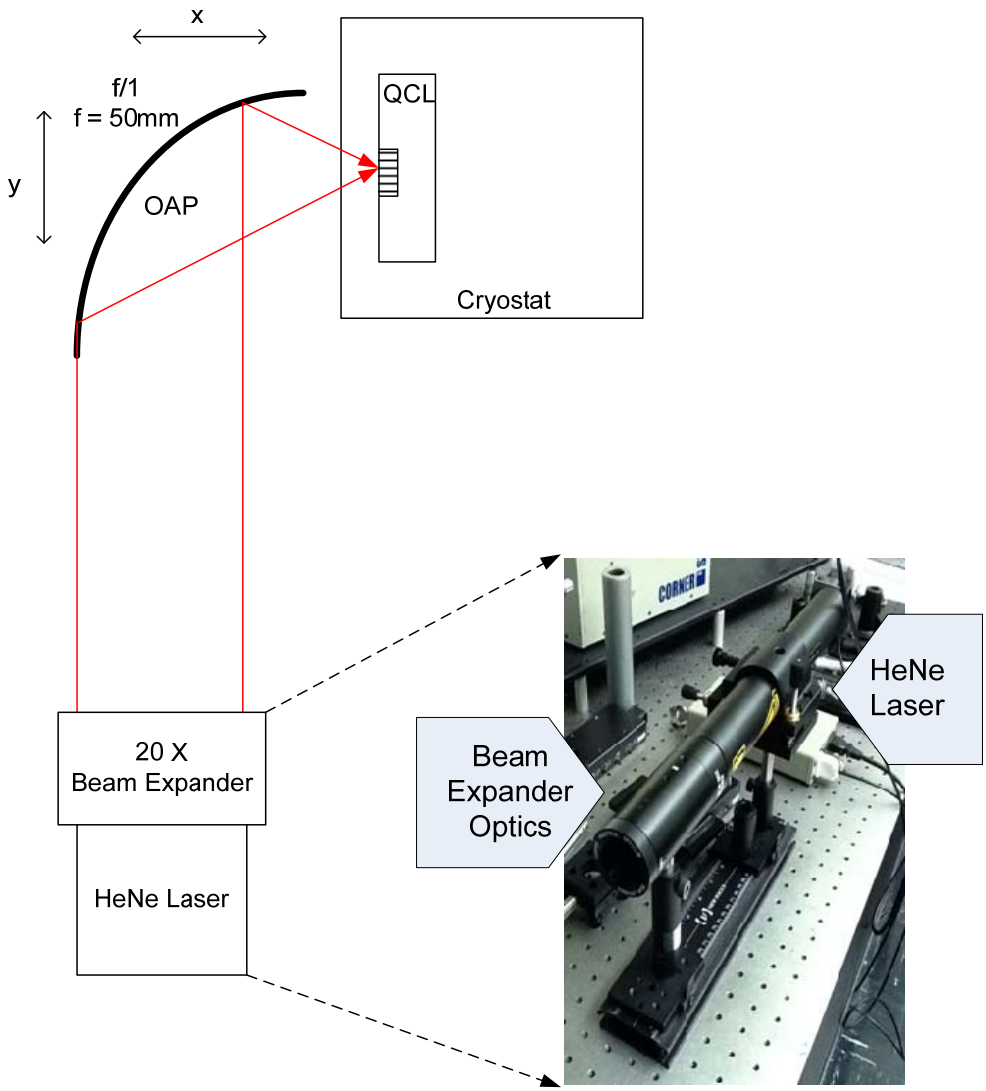

Figure 13. Collimation of the QCL. The OAP is mounted on a two-axis platform, as shown in the schematic. This allows the OAP to be translated in both x and y directions. A collimated commercial HeNe laser was used to collimate the QCL.

The second step involved the use of a flat front-plated gold mirror to direct the QCL beam into the external port of the FTIR spectrometer, as shown in Figure 14. This was achieved with the use of the in-built alignment laser of the FTIR spectrometer.

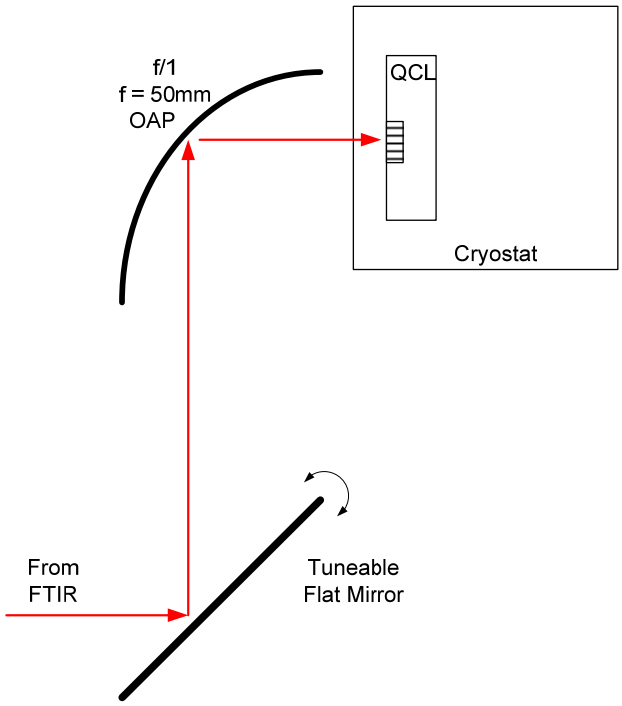

Figure 14. Directing the QCL into the FTIR Spectrometer. The alignment of the QCL beam into the FTIR is done by aligning the QCL axis with the red alignment laser from the external port of the FTIR.

B. SPECTRAL MEASUREMENT RESULTS AND ANALYSIS

For all measurements, the QCL was driven using an AVTECH pulsed laser diode driver, model AVO-6HZ-B, a laser driver designed to provide large current drive of up to 10 A with duty cycle of up to 5%. The detailed specifications of the laser driver are enclosed in Appendix A.

The FTIR spectroscopic measurement of the QCL was obtained by driving it at 1 kHz with a bias current of 2.7 A and a duty cycle of 0.5 %. The variation of the laser intensity as a function of signal spectral frequency is plotted in Figure 15. The peak intensity of the QCL was determined to be around 3.78 THz, or at wave number of about

126 cm^{-1} at the FTIR scan resolution of 1 cm^{-1}, which agreed with the manufacturer's specification. The full-width half-maximum (FWHM) spectral width of the QCL was estimated to be about 30 GHz from the plot.

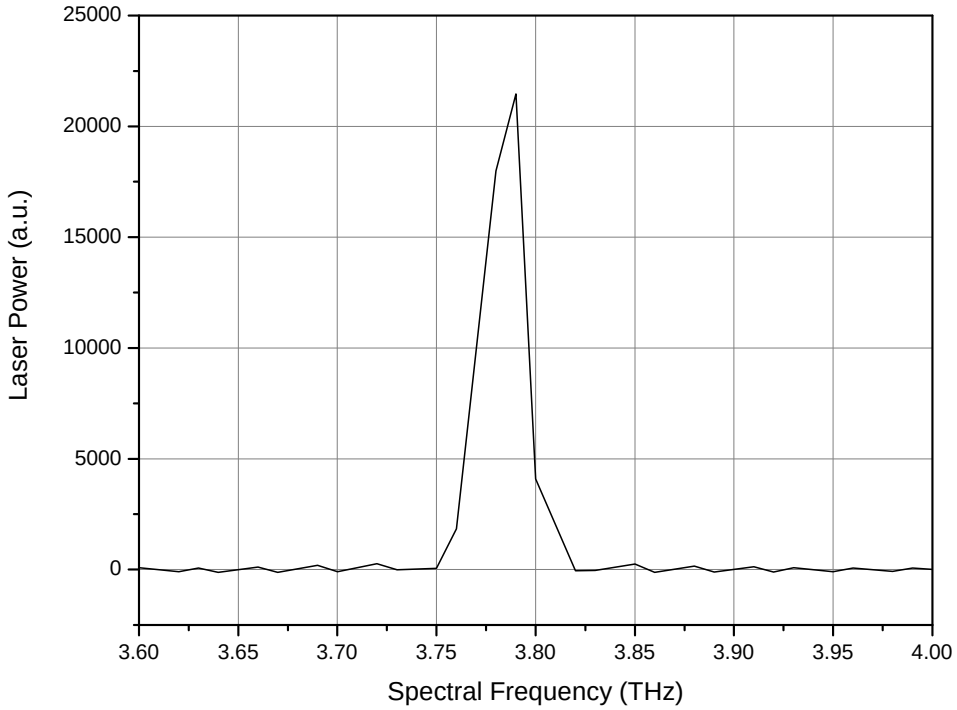

Figure 15. Measured laser power as a function of THz frequency.

C. POWER MEASUREMENT RESULTS AND ANALYSIS

The FTIR spectrometer was also used for investigating the power performance of the THz QCL. However, since the interferometric setup in the FTIR spectrometer was mainly designed to quantify a material's optical characteristics, its sensor output would not be providing true radiometric measurement. Instead, the measurement results would be in terms of a percentage of the flux directed at the material under test, in other words, the percentage transmittance and percentage reflectance. In the case of the QCL, which would be used as an external source, the flux magnitude measured would be in arbitrary units, as the FTIR sensor calibration is unknown.

The QCL was driven at 5 µs pulse duration for all power measurement experiments to prevent excessive power dissipation in the QCL. The pulse repetition frequency (PRF) and magnitude of the driving current were varied to determine the optimal drive conditions for the QCL.

The QCL output power was measured using the FTIR against an increasing drive current, and is shown in Figure 16. It was found to peak at around 2.7 A of drive current, which needed a drive voltage of about 55 V, and decreases rapidly thereafter. The behavior was replicated at a set of pulse repetition frequencies (PRFs).

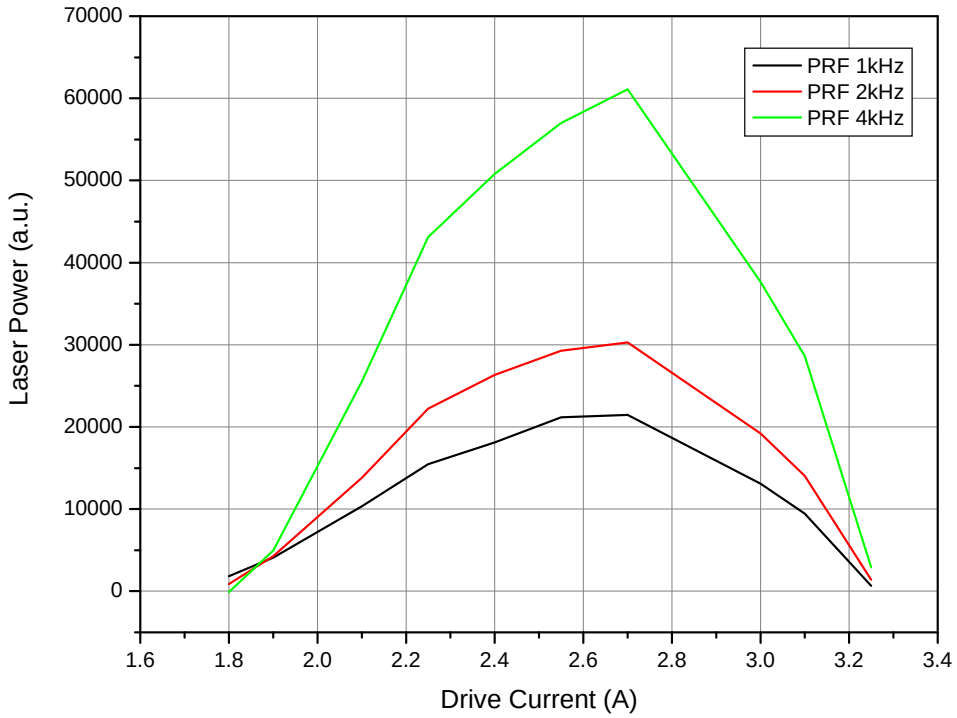

Figure 16. Measured QCL power as a function of drive current for a set of pulse repetition frequencies (PRFs).

As expected, the QCL output power was found to increase readily with increasing duty cycle by increasing the PRF at a constant pulse width, as shown in Figure 17, for the optimal drive current of about 2.7A. It was noted that the peak laser output power actually doubled every time that the PRF was doubled. This linear relationship suggested

that the heat build-up in the QCL cavity was being dissipated sufficiently, which prevented any degradation in the laser output performance. The experiment was conducted for the maximum allowed PRF of 10 kHz or a duty cycle of 5%, which was the limit for the laser driver system.

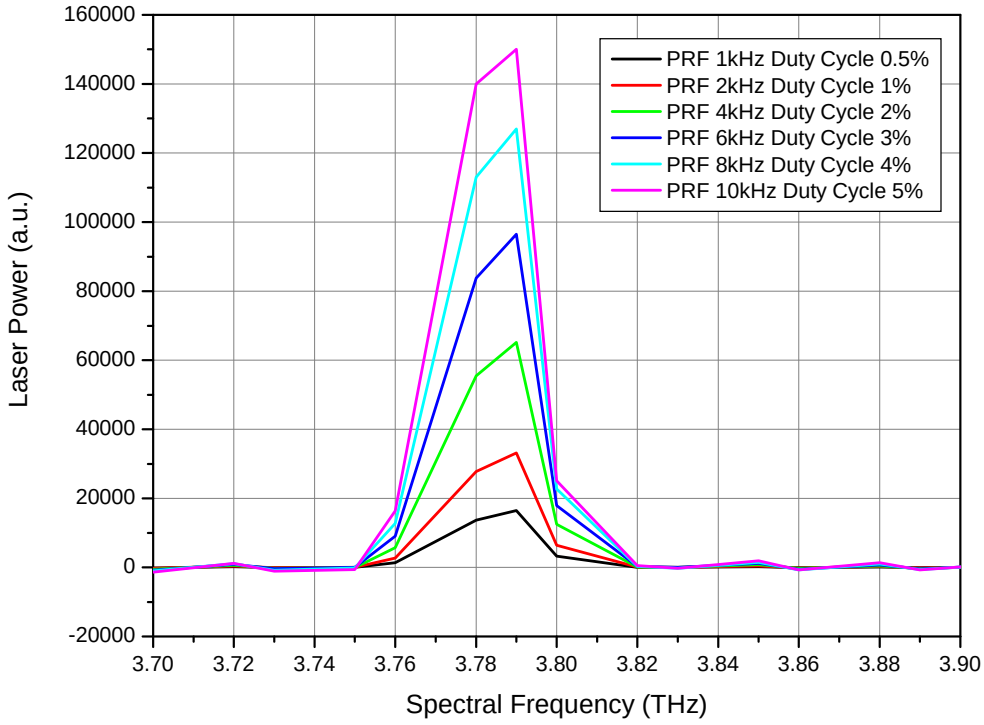

Figure 17. Measured QCL output power as s function of THz frequency for a set of duty cycles. Duty cycle was varied by increasing PRF at a constant pulse width of 5 µs.

D. THERMAL PERFORMANCE OF QCL

As mentioned earlier in Section C, the QCL output power was found not to be degraded with increasing PRF or duty cycle, which suggested that the rate of heat removal from the QCL was sufficient for the current drive conditions. The experiment was repeated with the monitoring of the initial[1] rise of the temperature of the cryostat assembly[2] when the QCL was driven at different duty cycle and the optimal drive current of 2.7 A. The results, as shown in Figure 18, demonstrated that the laser performance was not degraded, as the laser output power was shown (by the black dots) to be increasing linearly with increasing PRF (or duty cycle), while the cryostat temperature rose from about 14 K to 26 K.

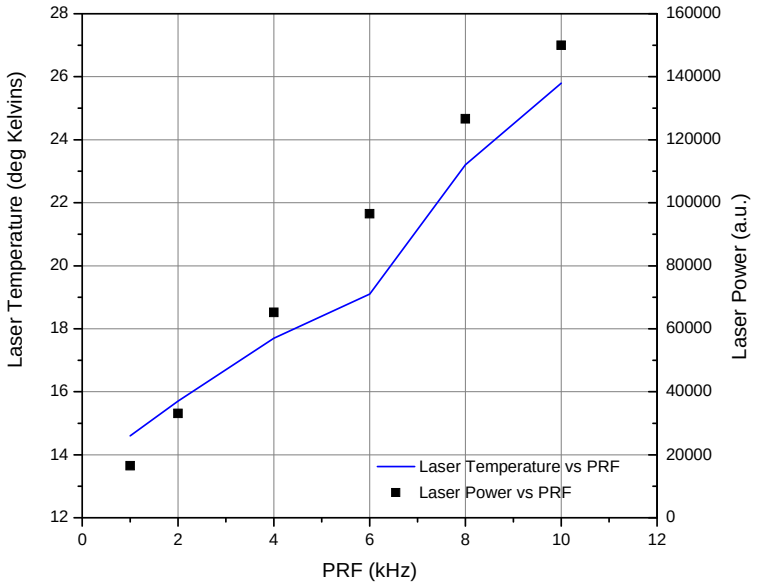

Figure 18. The laser power (measured in arbitrary units) and the temperature of the cryostat assembly plotted against the pulse repetition rates (PRF) used to drive the laser.

[1] Initial rise in temperature refers to temperature increase over the duration of data acquisition in the FTIR, which essentially was about 5 minutes.

[2] The cryostat assembly refers to the cold finger that the heat sink with the QCL was attached to within the cryostat. The temperature probe was not attached in direct contact with the QCL in this experiment.

THIS PAGE INTENTIONALLY LEFT BLANK

IV. TERAHERTZ IMAGING

This chapter details the experimental procedures in acquiring THz images in transmission mode, and the experiments conducted with the new QCL, together with a vanadium oxide based 160 x 120 microbolometer focal plane array camera from FLIR Systems. The optical setup for formation of the THz image in the conventional uncooled thermal camera will be described in the first part on the experimental setup. The electrical setup for synchronizing the camera receiver and the QCL source will be described in the second part of the experimental setup. The imaging results are then presented with detailed description of the experiment procedures and analysis of the images.

A. EXPERIMENTAL SETUP

1. Optical Setup

As opposed to the use of reflective optics, as shown by Lee et al. [11], two converging THz-transmissive lenses were used in the current THz imaging setup. The optical setup used by Lee et al. [11] comprised of two off-axis parabolic (OAP) mirrors and a single converging lens, and its purpose was to create the image of the object on the focal plane array (FPA) of the microbolometer camera. The proposed two-lens setup would also be imaging the object onto the FPA, as illustrated in Figure 19 and Figure 20, where Lens 1 would essentially serve the same purpose as the OAP mirrors in collecting and focusing the radiation from the QCL, and Lens 2 would served as the Si Lens in creating the image of the QCL onto the FPA.

Lens 1 is a f/3 (20 mm diameter, 60 mm focal length) Tsurupica lens, while Lens 2 is a f/1 (20 mm diameter, 20 mm focal length) Si lens. The back-illuminated object was placed along the optical axis, right after Lens 1, along the path of focusing laser power.

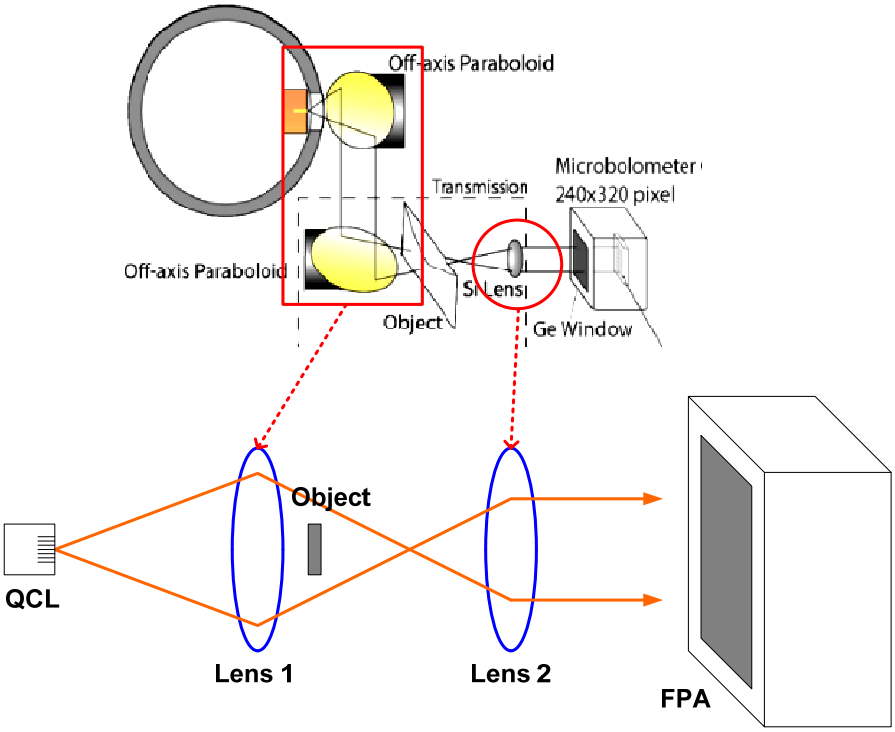

Figure 19. Schematic of the Optical Setup for THz Imaging. Two converging lenses were used, instead of reflective optics to form the image of the object onto the FPA.

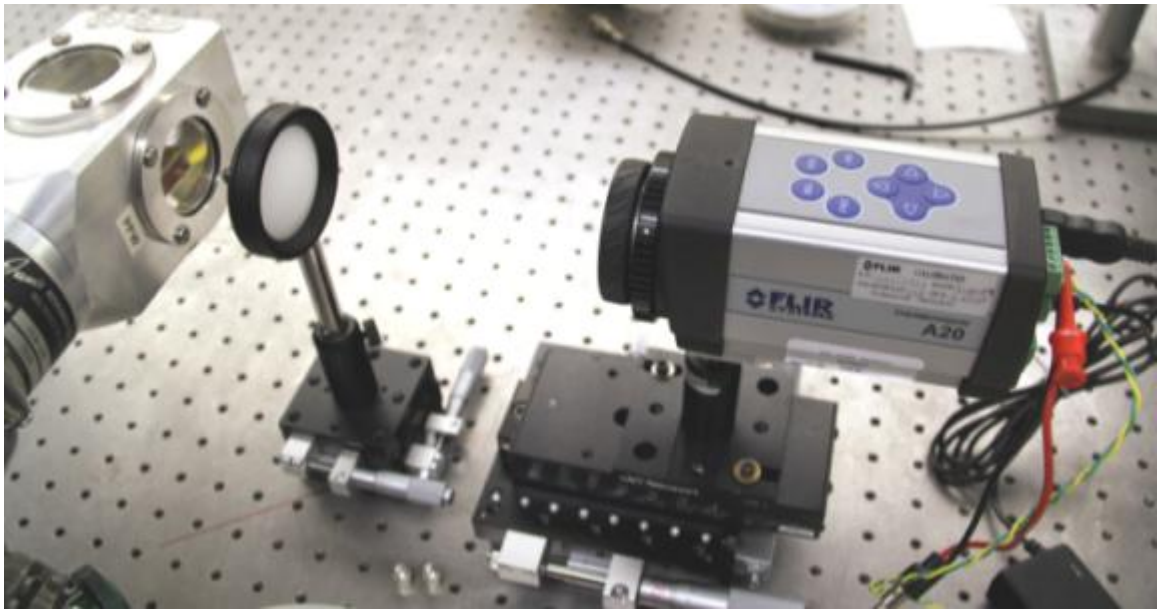

Figure 20. Picture of the Optical Setup for THz Imaging. Lens 1 is the visibly opaque (white) lens in front of the cryostat, and Lens 2 is the clear lens in front of the camera.

2. Electronics for Differential Imaging

Differential imaging requires the synchronization of the laser pulses with the camera integration duration, also known as the frame time [11]. This would help to eliminate undesired background thermal radiation that would have been sensed by the microbolometer sensor. The process required two operations, which included an operation to synchronize the camera frame time with the laser activation time, and a second operation to limit the laser pulses to within the single camera integration duration.

The current electrical setup included an integrated circuit (IC) of a binary counter (Model CDS4520B), an Agilent Pulse Generator (Model 8114A), a FLIR camera (Model A20M), and a high power laser diode driver system (Model AVO-6HZ-B), as shown in Figure 21.

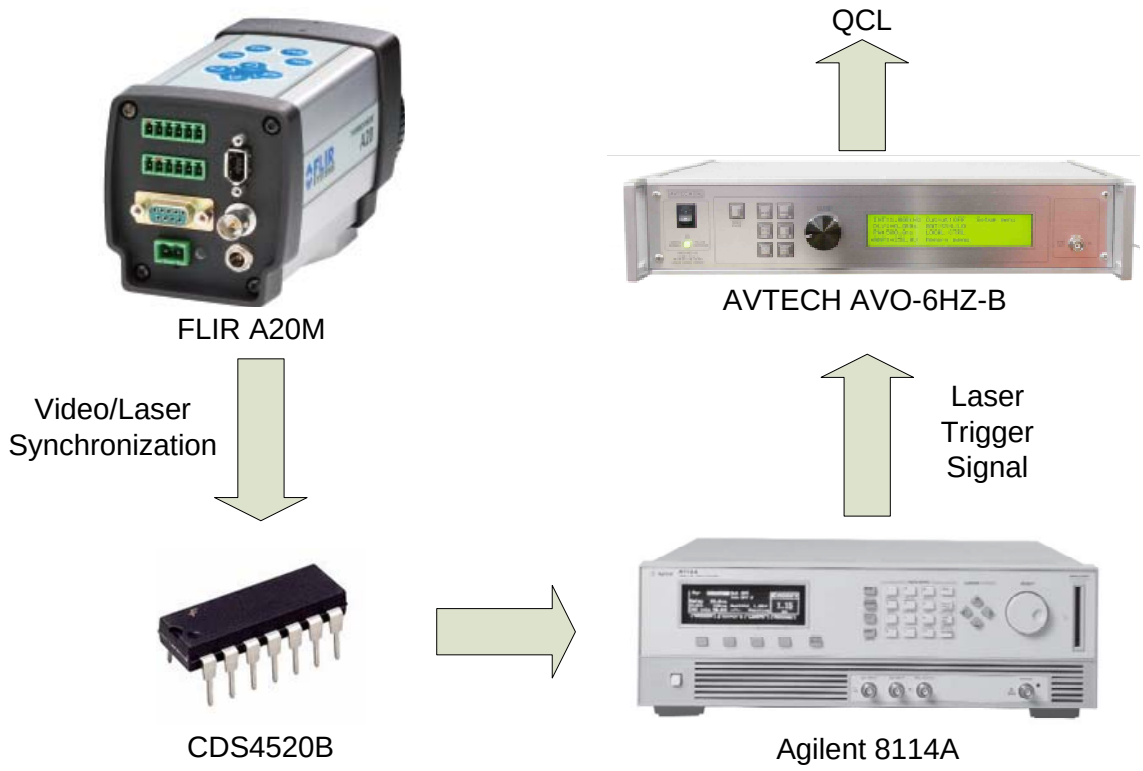

Figure 21. Electrical setup of the THz imaging system. A synchronization signal from the FLIR camera was extracted to generate synchronized laser drive pulses.

For the first operation to synchronize the camera frames with the laser activation, a synchronization signal for the video stream, known as the VSYNC signal, was extracted from the digital output port (Pin 4), as shown in Figure 22, of the FLIR A20M camera. This VSYNC signal could be used with delay or D flip flops to generate time-delayed synchronization signals for the laser activation. A commercially available binary counter integrated circuit (IC), CDS4520B, was used in this experiment. It is comprised of two identical, internally synchronous 4-stage up-counters, which are made up of D flip flops. It provided time delay in multiples of the frame duration, such as 2, 4, 8 and 16 times of the frame period. The VSYNC signal was fed into the ENABLE input (Pin 2) of one of the two up-counters as shown in Figure 22. For the A20M camera, the VSYNC signal was a negative pulse, so VSYNC signal was fed into Pin 2 of CDS4520B, while Pin 1 was held at ground potential (0 V).

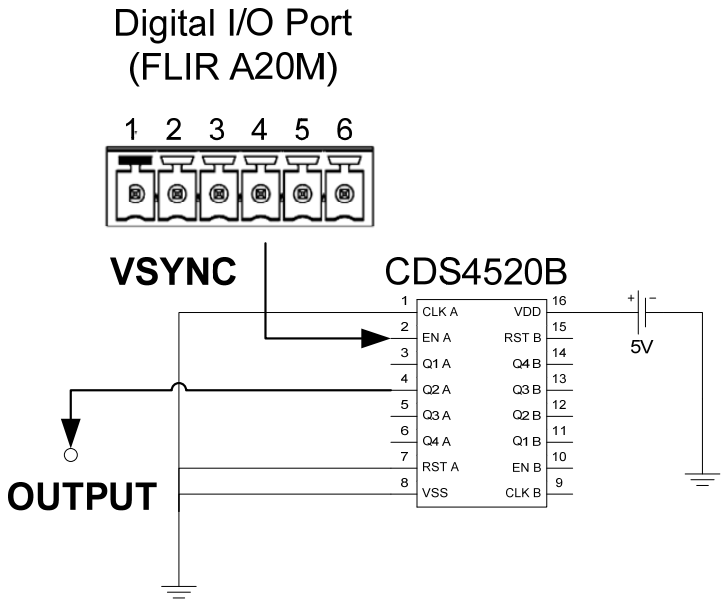

Figure 22. Schematic drawing of CDS4520B with VSYNC signal from the digital input/output port of the FLIR camera.

The output signals from Q1A to Q3A are shown in Figure 23, with Q1A signal at 15 Hz (period of 67 ms), Q2A at 7.5 Hz (period of 133 ms), and Q3A at 3.75 Hz (period

of 267 ms), respectively. The fourth signal Q4A at 1.875 Hz (period of 533 ms) was not shown due to the limited number of probes to the display oscilloscope.

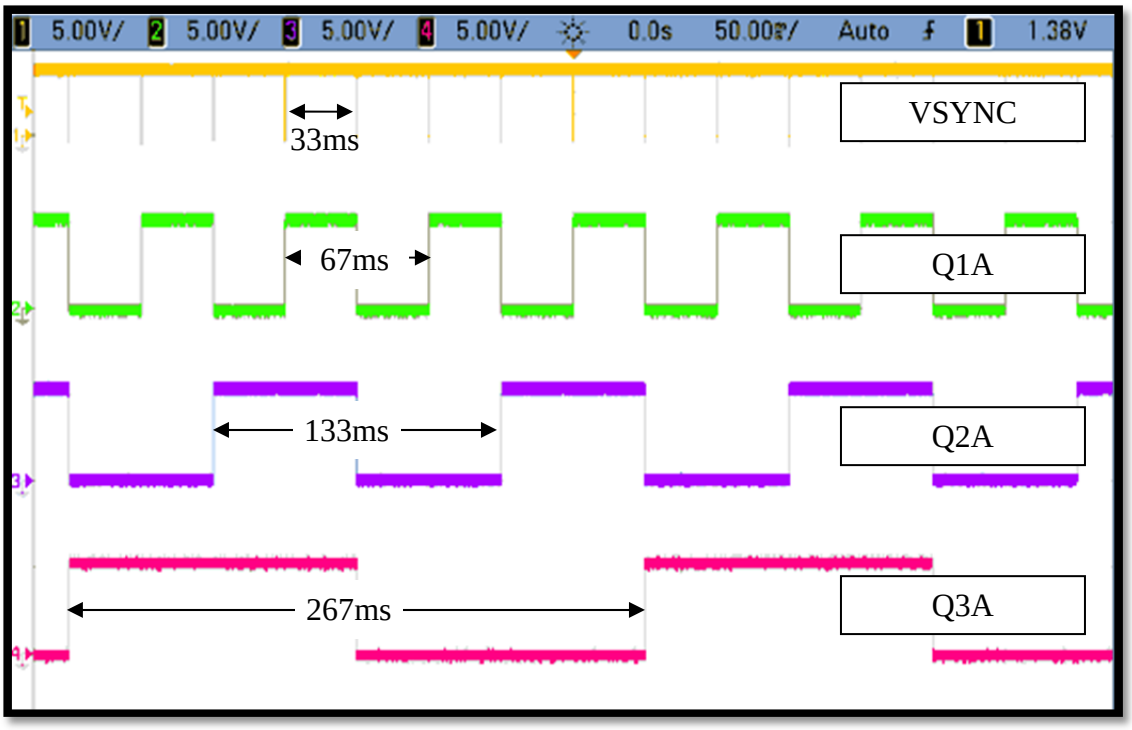

Figure 23. Different delayed signals from CDS4520B dual counter IC, as generated from the VSYNC signal out of the FLIR camera.

The second operation of limiting the laser pulses to within a single frame duration was accomplished with the use of another pulse generator, the Agilent Pulse Generator (Model 8114A). Output Q2A or Pin 4 of the CDS4520B chip was chosen to drive the next stage, as it provided a delay of four (4) frame periods (which was more than the three frames demonstrated by Lee et al. [8]). This would be sufficient for the discharge of the THz laser signal in the focal plane elements. More details of the triggering requirements are elaborated in the next section on differential imaging. Five hundred (500) single pulses of laser triggering signals were generated at 50 μs intervals (or 20 kHz), as shown in Figure 24, which translated to effective laser on time of about 25 ms.

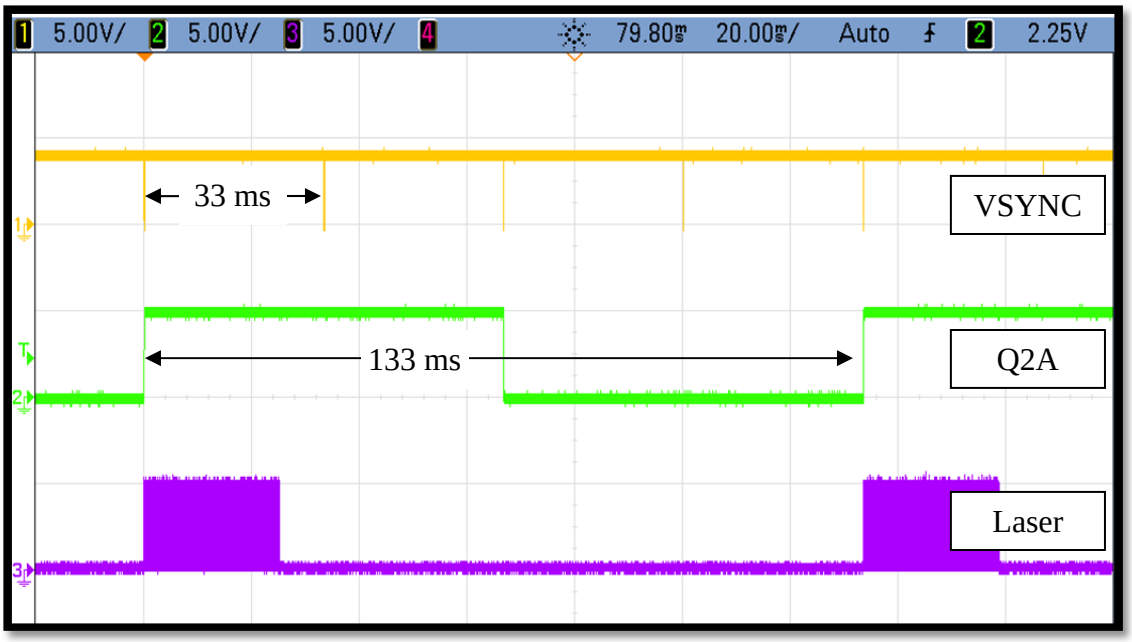

Figure 24. Laser trigger signal generation with Agilent pulse generator (Model 8114A).

B. TERAHERTZ TRANSMISSION MODE IMAGING RESULTS

Terahertz (THz) transmission mode imaging experiments were performed using the optical setup and electrical setup described in the previous section, as well as test subjects placed just after the Lens 1. The laser was triggered with the synchronization setup at a frequency of about 7.5 Hz, which was one quarter of the camera frame rate of 30 Hz. The drive current amplitude was set at maximum of 2.7 A, corresponding to a bias voltage of 55 V. Up to 500 single pulses of laser signals, with 5 μs pulse width each, were triggered to illuminate the test subject or target within one camera integration frame time.

The image of the laser beam without any test subject was captured as shown in Figure 25. Concentric rings were observed in the image, and the amount of power distributed among the rings was significant, as shown by the line profile in Figure 26. Adam et al. [18] claimed that the rings were a result of far field interference caused by the laser radiation from various facets of the laser bar itself, as shown by the image that they had captured in Figure 27.

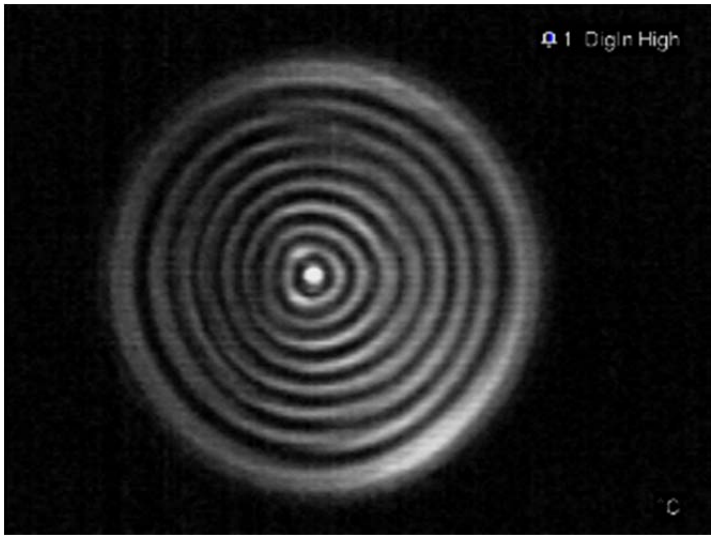

Figure 25. Imaging of the QCL using two spherical lenses, as described in the optical setup.

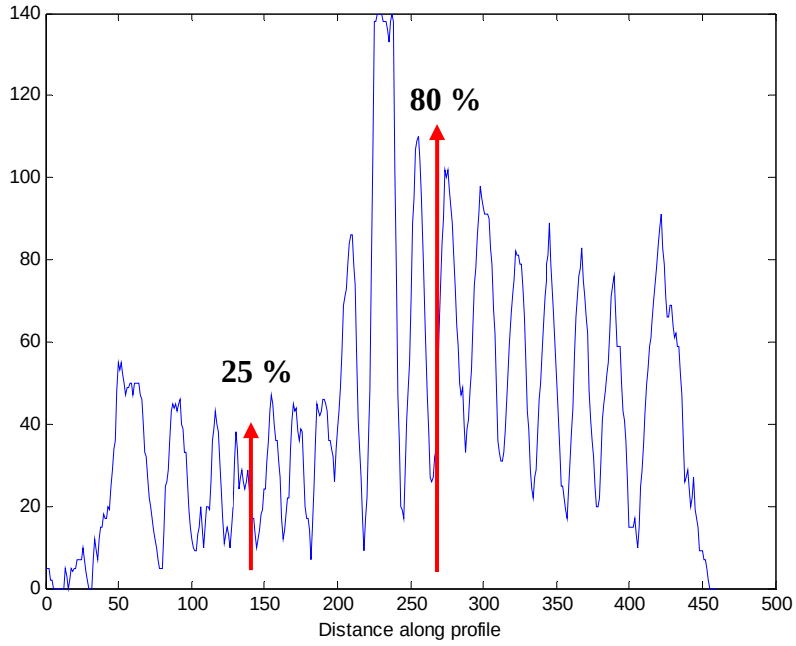

Figure 26. Line profile across the center of the QCL image. The heights of the peaks range from 25 % to 80 % of the central maxima.

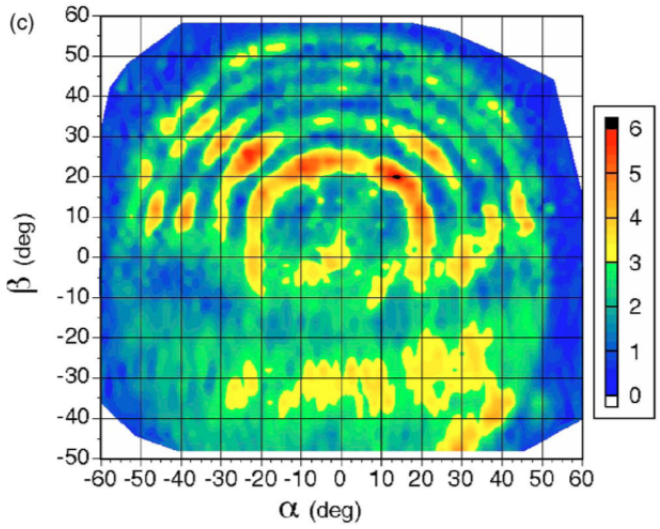

Figure 27. An image of the emission pattern for a QCL with length 1500 μm, width 25 μm, thickness 10 μm, and emission wavelength 109.1 μm. (From [18]).

Orlova et al. [19] modeled a long laser with an antenna model, and concluded that the angular size of the laser output is more sensitive to the length of the laser than the size of the aperture. Their modeling results, as shown in Figure 28, were consistent with the measured results from Adam et al. [18].

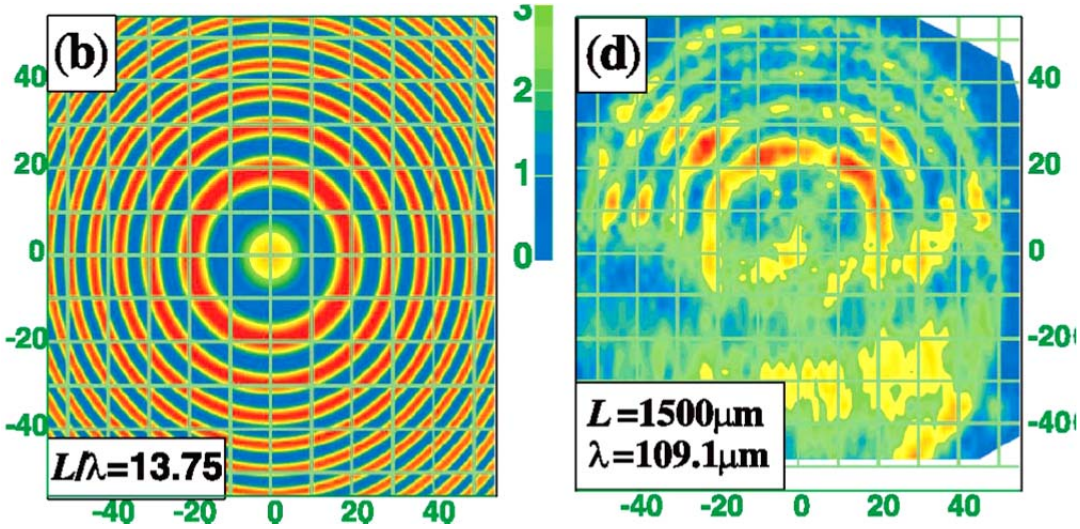

Figure 28. Modeling and simulation result (left) versus the measured result (right). (From [19]).

A small knife blade wrapped in opaque tape of plastic material was used as the first test subject, as shown in Figure 29(a). The portion of the metallic blade under the white plastic tape was not visible under normal reflected visible light, nor was it visible when back-illuminated with strong visible light. However, the edges of the partially hidden knife blade were clearly seen under THz back-illumination, as shown in Figure 29(b).

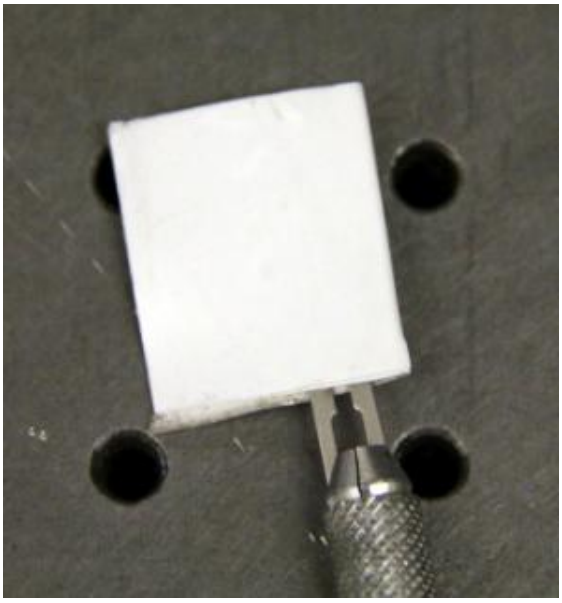

(a)

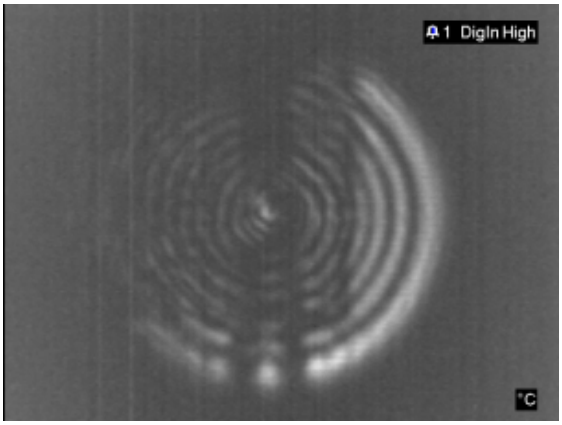

(b)

Figure 29. Imaging of a knife blade wrapped in white plastic tape. (a) Digital image of the knife blade wrapped in white plastic tape. (b) THz QCL illuminated image of the knife blade captured with the FLIR microbolometer camera.

A second test subject was configured using a thin piece of polystyrene foam, also commonly known as Styrofoam, with a similar knife blade inserted in the middle, as shown in Figure 30(a). Similarly, the knife blade was not visible under strong visible light, but the edges were distinct from the background under THz illumination, as shown in Figure 30(b).

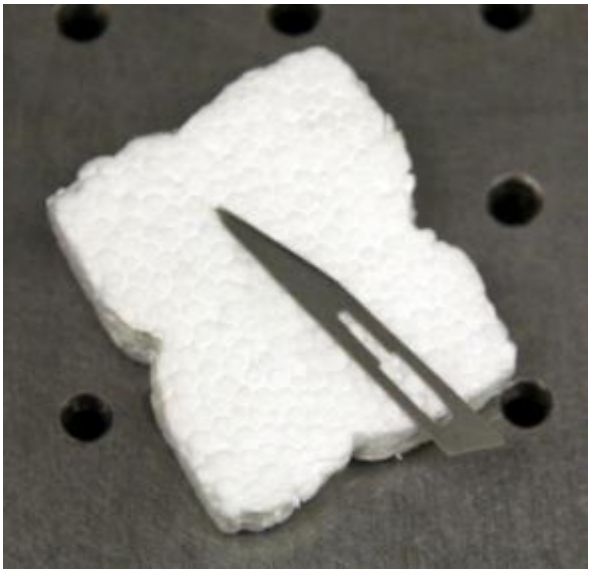

(a)

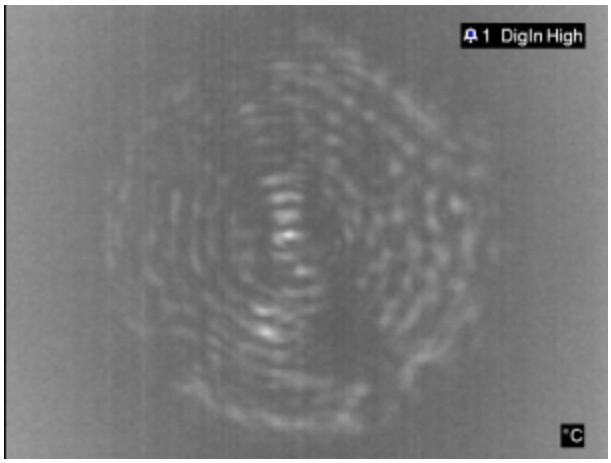

(b)

Figure 30. Imaging of a knife blade embedded in a piece of styrofoam. (a) Digital image of the knife blade to be embedded into a piece of styrofoam. (b) THz QCL illuminated image of the knife blade captured with the FLIR microbolometer camera.

All the THz images presented show a whitish background, which was due to the relatively weak THz signal and the camera's auto-shutter function. The camera's auto shutter function performed constant adjustment of the temperature sensitivity range, depending on the image intensity or the radiance received. Since the THz signal was not significantly stronger than the background, low contrast was shown. Differential imaging process of background subtraction would be beneficial in improving the contrast by removing this relatively strong background. This will be presented in the next section.

C. DIFFERENTIAL IMAGING RESULTS

Differential imaging has been employed to eliminate the background infrared contribution to each terahertz image, as was done by Lee et al. [8]. The current active terahertz imaging setup has been designed to operate with synchronized laser firing at 1 times, ½ times, ¼ times, ⅛ times and 1⁄16 times of the video frame rate. Hence, for a video frame rate of 30 Hz, the laser would be activated at either 30 Hz, 15 Hz, 7.5 Hz, 3.75 Hz, or 1.875 Hz, respectively.

Active terahertz images were recorded with the FLIR A20M microbolometer camera into an AVI sequence for laser activation rates of 15 Hz, 7.5 Hz and 3.75 Hz, respectively. The AVI sequences were then segmented into individual red-green-blue (RGB) images using National Instruments Vision Assistant (2010 version) program, as illustrated in Figure 31, where a short AVI sequence of ten (10) frames for each activation rate are shown. For each activation rate, the first frame is the top left image, continuing across till the 5^{th} frame, followed by the 6^{th} to 10^{th} frame on the second row. The same number of laser pulses (which was 1,000 pulses of 5 μs pulse width) was programmed at each laser activation time. The laser signal was apparent in each AVI sequence, occurring at the second frame for 15 Hz and 3.75 Hz, and at the first frame for 7.5 Hz. It was noted that the signal decay time constant was estimated to be about three (3) video frame durations as shown in Figure 31(b). Hence, by taking the difference of the laser illuminated image and the background (i.e., in the absence of terahertz laser energy) image, the infrared energy contribution from the background at around 300 K would be minimized.

Considering the laser activation rate of 7.5 Hz, as shown in the AVI sequence in Figure 31(b), the RGB images were first converted to gray level, as shown in Figure 32. Lines of distinctly different intensity levels were apparent in these two images, and the maximum pixel values were determined to be 254 and 197 for the laser illuminated and the background images, respectively.

The difference image, as shown in Figure 33, was void of the vertical lines. The edges of the target object, which was a small utility knife, half wrapped with opaque tape, were clearly seen in the processed image.

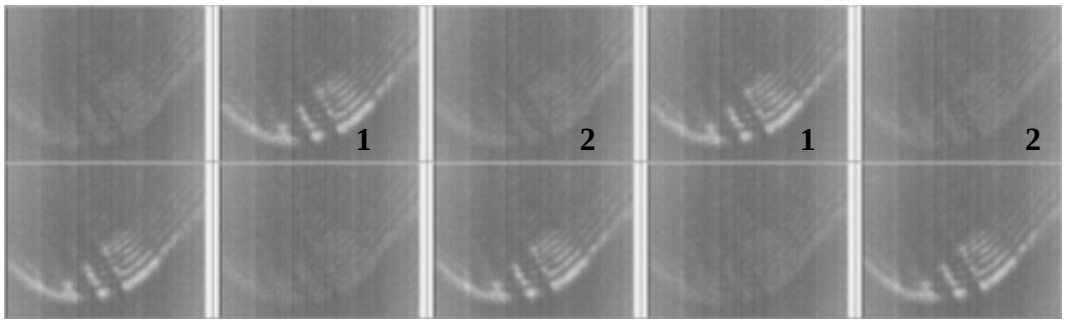

(a) 15Hz

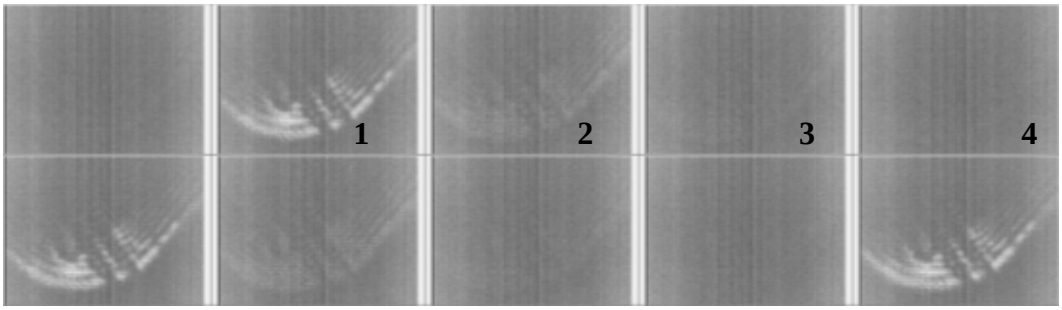

(b) 7.5Hz

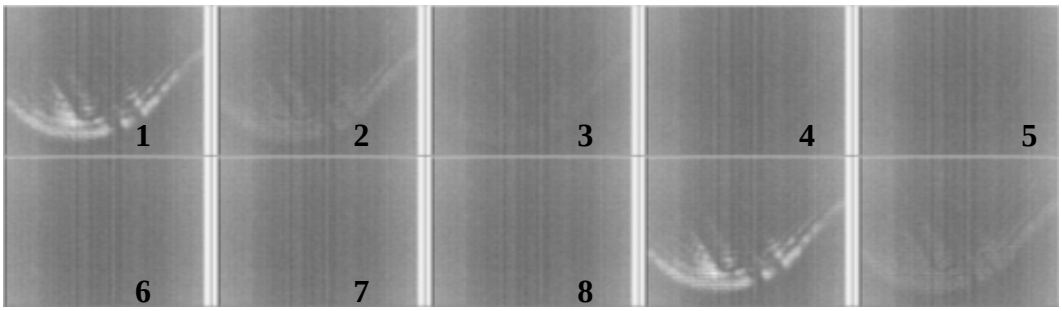

(c) 3.75Hz

Figure 31. Active terahertz images captured with different laser activation time durations of (a) 15 Hz; (b) 7.5 Hz; and (c) 3.75 Hz.

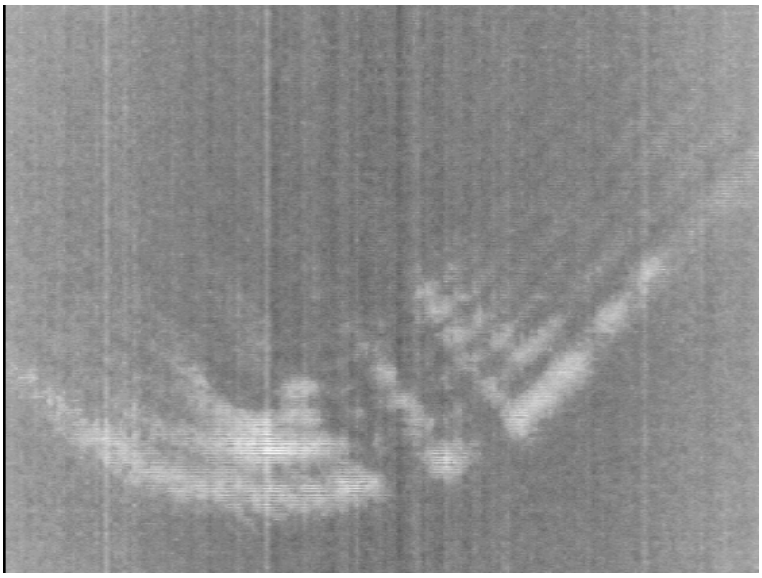

(a) Laser Illuminated

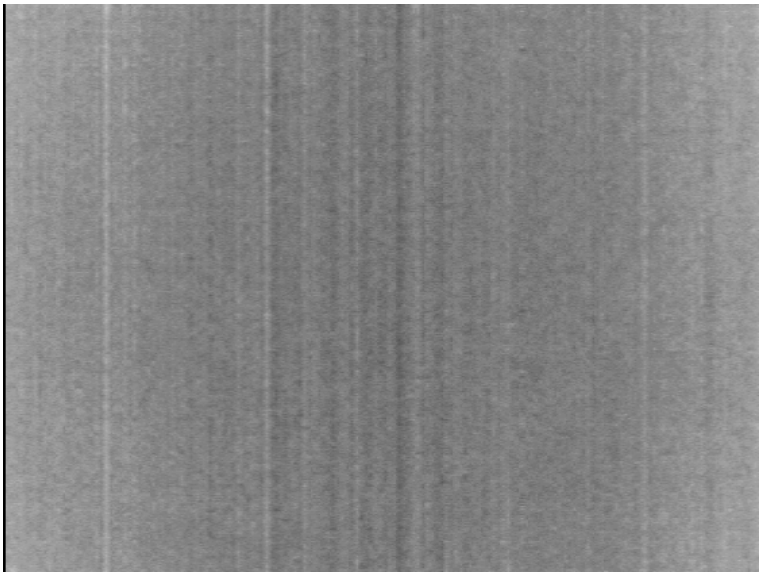

(b) Background

Figure 32. (a) Laser illuminated image (Frame #1) and (b) background image (Frame #4) from the AVI sequence at laser activation rate of 7.5 Hz.

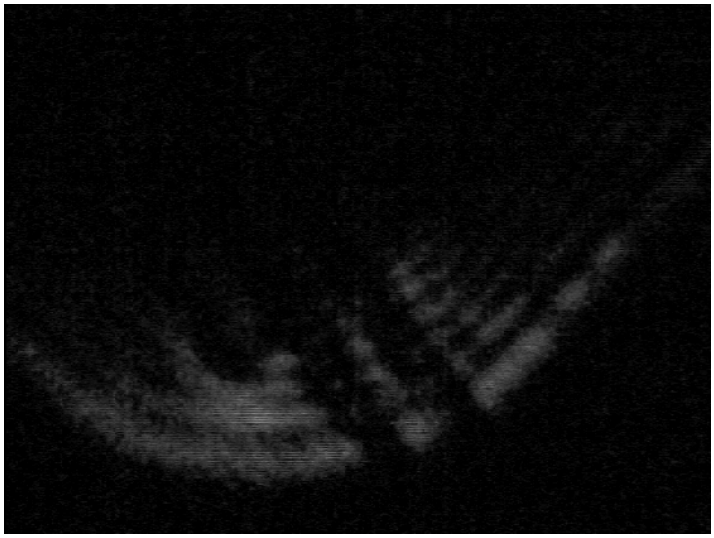

Figure 33. Difference image processed from the AVI sequence at laser activation rate of 7.5 Hz.

D. IMAGE PROCESSING

In the experiments, images from the FLIR A20M 160 x 120 elements microbolometer focal plane array camera were recorded in an audio-video interleave (AVI) sequence, instead of individual images. In the AVI sequence, each image is in Red-Green-Blue (RGB) format, with a size of 640 x 480 pixels and encoded at 16-bit resolution. Vision Assistant 2010 program from National Instruments was used to extract the images from each AVI sequence, and saved in 8-bit unsigned integer format. The RGB images were converted to gray level for processing, as the color information was not significant in terahertz imaging application.

Post-acquisition image processing was essential due to a number of reasons. First of all, the automatic shutter in the FLIR A20M camera performs a calibration for the camera pixels every few minutes, which effectively changes the background temperature sensitivity range, and the camera images would look different owing to any slight change in the background flux level. Secondly, the weak THz radiation received by the sensor means a poor signal-to-noise ratio, thus the noise level is significant in the THz images captured.

For the first issue, differential imaging would aid in eliminating unwanted background, but it would also result in very dark images. Image contrast enhancement techniques would aid in improving the contrast of these dark images to enhance the appearance of the target. For the second issue, spatial filtering techniques would aid in eliminating the speckle type of noise present in the THz images.

In automated imaging system, feature extraction algorithms such as edge detection or thresholding algorithms could be used to enhance the comprehension of the targets within an image. However, the THz images are much less intuitive, as they comprised of multiple parameters, such as different materials have varying reflectances and transmittances, and all information would be essential in identifying the material under test. Hence, feature extraction algorithms were not applied in this research.

1. Image Contrast Enhancement

Contrast is the difference in visual properties that makes an object distinguishable from other objects and background. One commonly used feature of an image is its histogram, which can be used to describe the amount of contrast. Since contrast is a measure of the difference in brightness between light and dark areas in an image, broad histograms will imply an image with significant contrast. On the contrary, narrow histograms reflect less contrast and may appear flat or dull. The images of the laser illuminated target, background, and the computed difference are shown in Figure 34, along with the corresponding histograms. The histograms of the first two images were centered at the middle intensity range of 100 to 150, which was associated with the auto-shutter, auto-gain adjustment of the FLIR camera. The difference image looked darker, owing to the subtraction of the background intensity from the laser illuminated target. As shown in the histogram for the difference image, the bulk of the pixel elements now registered much smaller intensity values. This skewed histogram could be enhanced further to brighten the image.

There are two common ways to improve an image's contrast in MATLAB, mainly by manipulating its histogram: (1) Stretching the intensity distribution; and (2) Equalising the distribution of intensities to utilize the full range.

For the first technique of histogram stretching, each pixel value (I) is 'stretched' to its full range, which was 0 (I_{min}) to 255 (I_{max}) for the unsigned 8-bit integer format for the THz image. Each pixel (J) in the contrast stretched image of the laser footprint in Figure 35 appeared much brighter than in the original image, owing to the stretching of the pixel values to higher intensity levels, according to the formula

$$J = 255 \times \frac{I - I_{min}}{I_{max} - I_{min}} . \quad (4.1)$$

The second technique of histogram equalization enhances contrast by scaling the targeted histogram uniformly to enhance contrast. For the THz image in Figure 36, half of the total number pixels with intensity levels at the lower end of the histogram were redistributed across the entire 8-bit depth, such that the originally bright spots appeared much brighter. This intensity scale could also be adjusted manually by using *imadjust* function, so as to enhance the brightness of the desired "darker" portion of the image. The image in Figure 37 shows the effect of enhancing the darkest 30% of the image by manually "shifting" its histogram to the entire range.

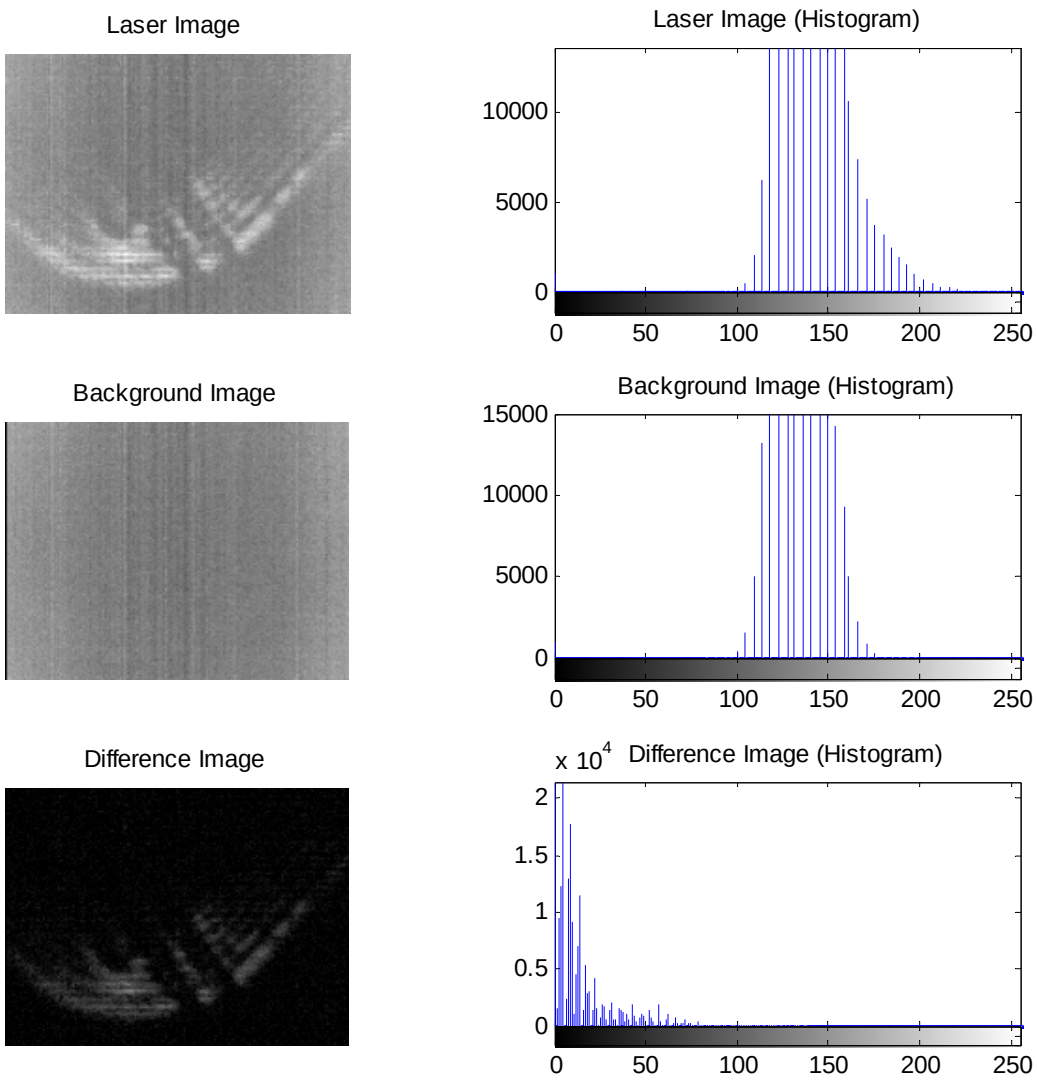

Figure 34. Eight-bit intensity images of the laser illuminated target, background, and the computed difference, together with the corresponding histograms.

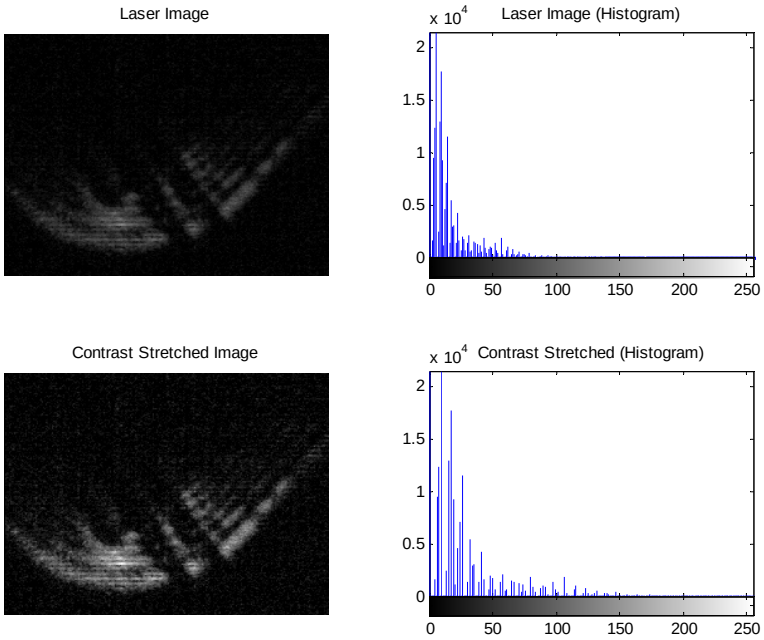

Figure 35. Contrast stretching technique. The histogram of the enhanced image is stretched, such that the stretched image shows a brighter laser footprint.

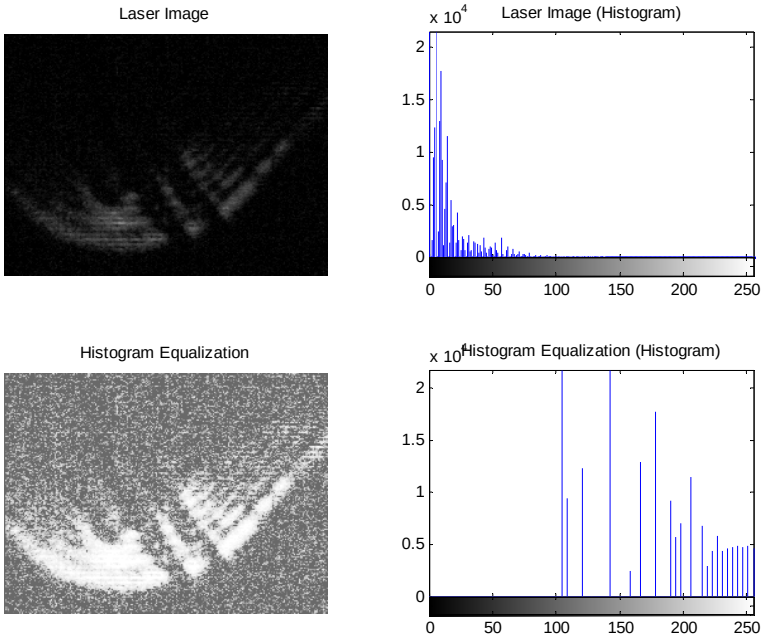

Figure 36. Histogram equalization technique. The histogram of the enhanced image is stretched, such that half of the pixels with lower intensity were redistributed across the whole histogram.

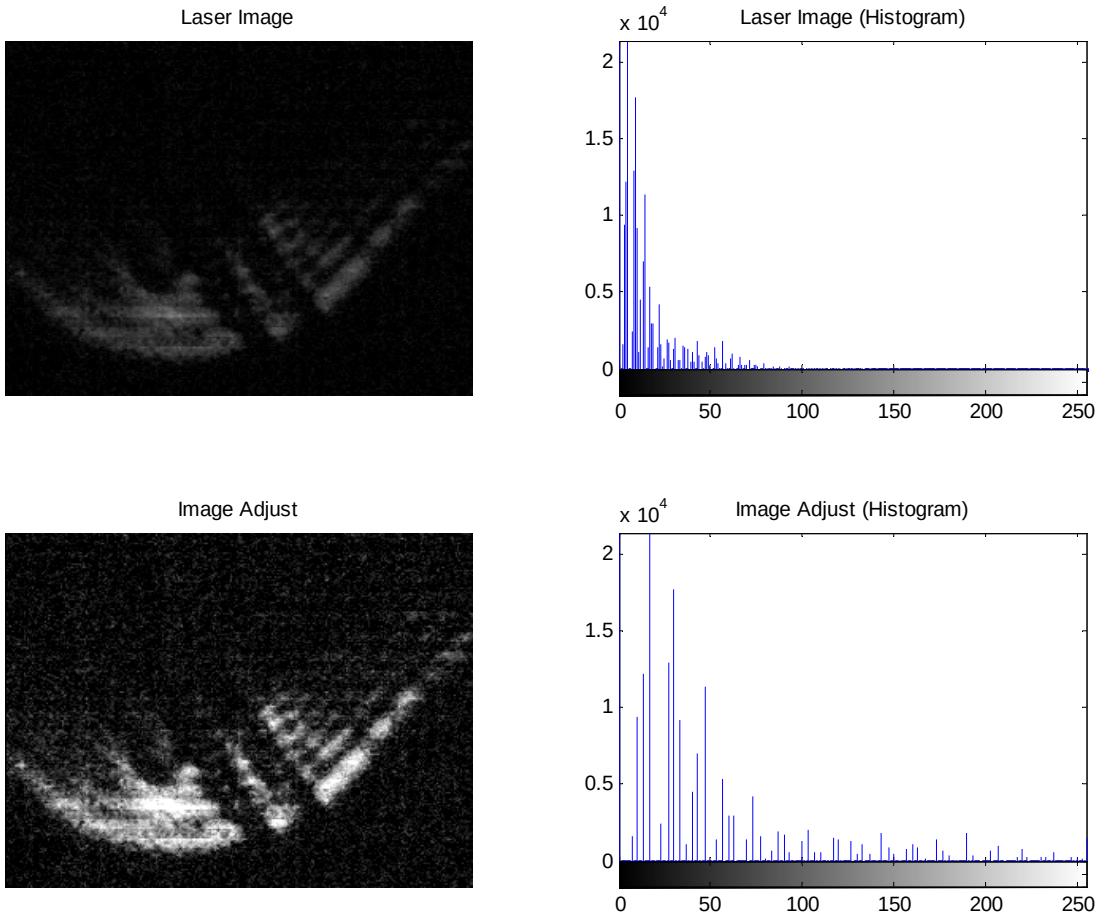

Figure 37. Manual adjustment technique. The histogram of the enhanced image is stretched, such that the pixels with intensity levels below 30% of the maximum were redistributed.

2. Spatial Filtering

Spatial filtering is the optimal technique in restoring the image distorted by random noise, which has been observed in the terahertz images after difference processing. The random noise can be seen as spots in the difference image presented in Figure 38, as well as the peaks between 0 and 50 in the histogram, which represent the numerous random spots of low intensity (between values of 0 to 50 in the 8-bit image). Averaging filter, median filter and Wiener adaptive filter are common spatial filters that can be applied.

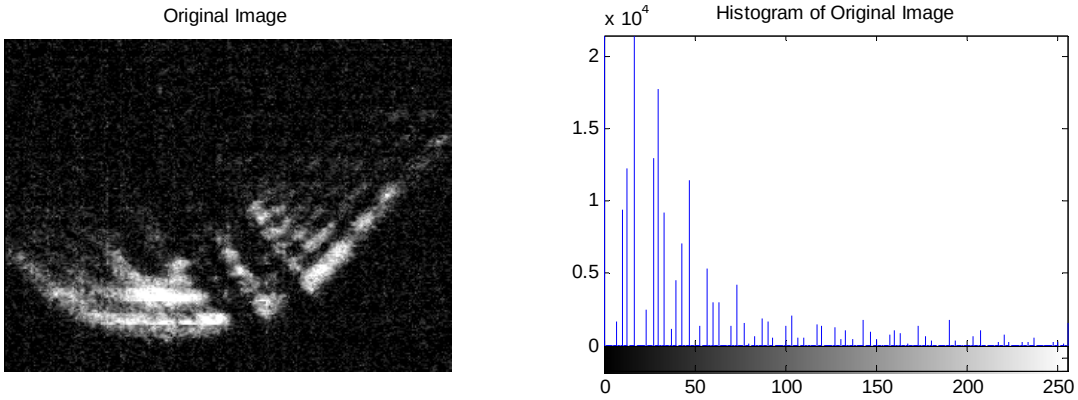

Figure 38. The original difference image with its associated histogram.

Averaging filter is a linear filter commonly used to reduce the graininess of an image, such as speckle noise. One disadvantage is that high frequency information or sharpness of the image could be lost in the filtering, resulting in softer edges, as shown in Figure 39.

Median filter is an effective filter for highly varying noise, such as salt and pepper, where noise intensity can vary between the two extreme ends. Such noise will not be totally removed by an averaging filter, but can be very effectively alleviated by the median filter. For the THz image used in this image processing algorithm, median filtering did not remove significant amount of the noise, as shown by the relatively high peaks in the histogram in Figure 40, which are comparable to that in the histogram of the original image.

Wiener filter is a well known approach to linear image restoration. This type of low pass filter is effective in reducing the effects of Gaussian white noise, and it is adaptive in the sense that it tailors itself to the local image variance, such that if the variance is large, it minimally smoothes the image, but does the opposite if the variance is small. For the THz image used in this image processing algorithm, Wiener filtering showed similar results to the averaging filter, as shown in Figure 41.

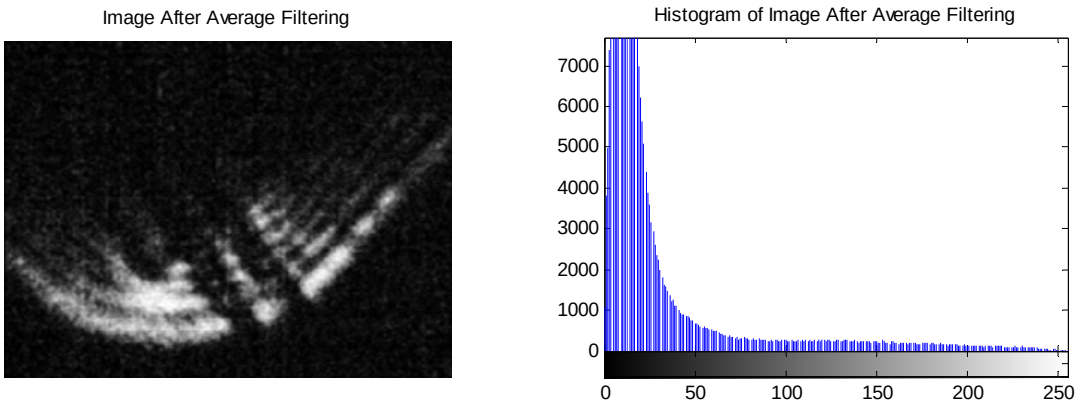

Figure 39. The original difference image after average filtering with its associated histogram.

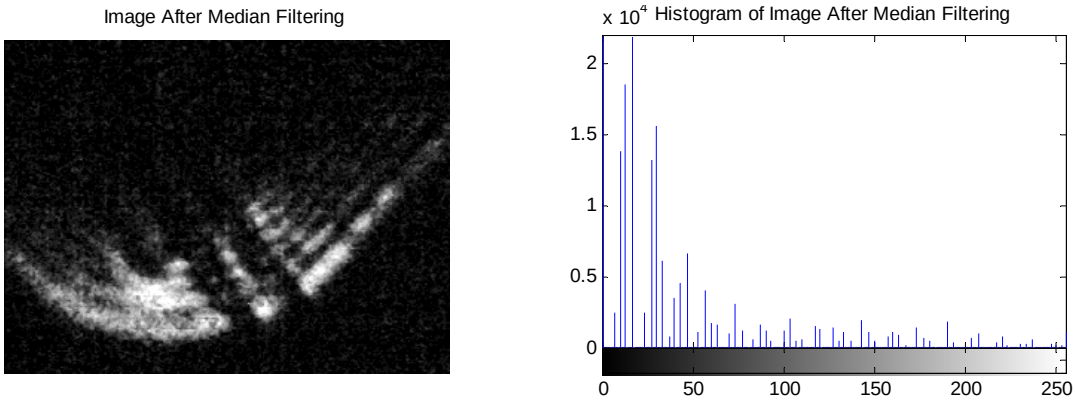

Figure 40. The original difference image after median filtering with its associated histogram.

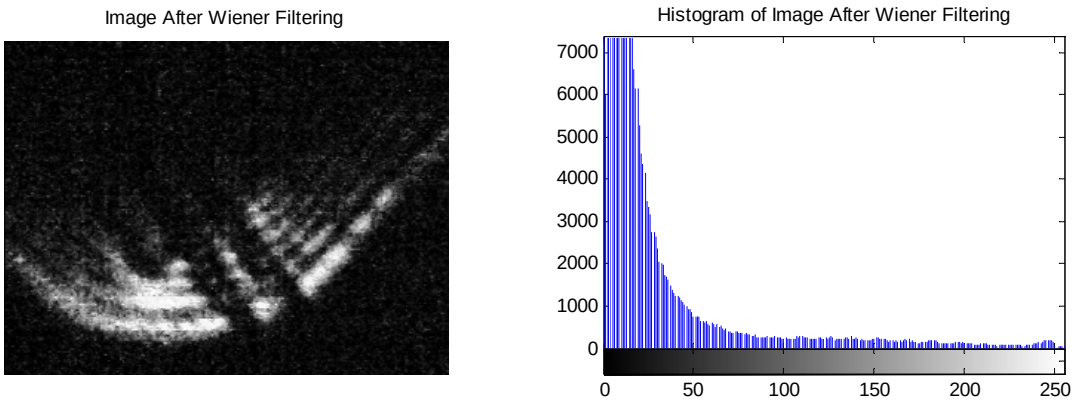

Figure 41. The original difference image after Wiener filtering with its associated histogram.

V. CONCLUSIONS AND RECOMMENDATIONS

A. CONCLUSIONS

A new high power terahertz quantum cascade (QC) laser has been acquired and characterized using a terahertz-optimized FTIR spectrometer. An f/1 off-axis parabolic mirror (OAP) was used to collimate the highly divergent laser beam into the external port of the FTIR. The operating spectral frequency of the QCL was determined to be about 3.78 THz, as per manufacturer's specification, and the laser power was measured to be a few orders of magnitude higher than the previous QCL used in past experiments. One contributing factor for the much higher magnitude other than the high power output design of the new laser is the modified alignment of the OAP mirror to place the laser emitter right at its focal point, which would have reduced the divergence of the QCL significantly. A much larger copper heat sink was used to couple the laser assembly into the cryogenic chamber to help dissipate the heat conductively, and optimal laser performance was found to be sustainable up to the limits of the laser driver.

The terahertz imaging setup was configured for differential imaging process. This was achieved by synchronizing the laser activation with the camera integration timing, and reducing the frequency of laser activation to one out of every four (4) camera integration intervals. This allowed the terahertz energy within each laser-illuminated camera frame to be dissipated sufficiently, as the signal decay time constant was determined to be between two (2) and four (4) standard frame periods, or between 67 ms to 133 ms. A differential imaging process was then completed by subtracting the background camera frame (or the fourth frame) from the laser-illuminated frame (or the first frame). The difference image was found to be void of infrared background noise, as well as reduced fixed pattern noise.

Image processing algorithms such as contrast enhancement and spatial filtering were developed in Matlab to improve the clarity of the images. Enhancing the contrast did help to make the THz images more intuitive, with sharpened edges of the target.

B. RECOMMENDATIONS

Terahertz imaging has been explored extensively in transmission mode, where the signature of a target is primarily determined by its opacity to terahertz radiation, as well as the contrasting transmission of terahertz radiation through its surroundings. This research has been focused much on the characterization of a higher power QCL source, and improvement to the existing imaging setup, as well as development of image processing algorithms to enhance the terahertz images due to the inherently small magnitudes of the detected terahertz radiation.

One area of research that could be explored would be reflective mode imaging, which is highly dependent on the reflectance of the materials and the respective background. Reflective mode imaging would have higher pay-off compared to transmission mode imaging, as the co-location of the source and receiver would benefit stand-off imaging applications. The main challenge behind reflective mode imaging would be the source power budget, which would have to be much higher due to the need to cater for greater atmospheric propagation loss, as well as dispersion loss.

APPENDIX A

Specification of AVTECH AVO-6HZ-B Laser Diode Driver

The key specification for the high power laser diode driver from AVTECH, Model AVO-6HZ-B, is provided as follows:

AVTECH AVO-6HZ-B	
Maximum Amplitude	10 Amp
Pulse Width (FWHM)	50 ns to 50 μs
Maximum PRF	100 kHz
Maximum Duty Cycle	5 %
Output Impedance	11 ohm
Trigger Output	Externally Triggered with TTL pulses (3 to 5V, more than 50 ns period)
Sync Output	3 V, 100 ns
Gate input	Synchronous or asynchronous, active high or low, switchable

THIS PAGE INTENTIONALLY LEFT BLANK

APPENDIX B

Image Processing Code in MATLAB

Image Contrast Enhancement

```
% Laser >> 'test0001.bmp';  Background >> 'test0004.bmp

L = imread('test0001.bmp');
Lg = rgb2gray(L);

B = imread('test0004.bmp');
Bg = rgb2gray(B);

Dg = Lg - Bg;

figure (1)
subplot (3,2,1); imshow(Lg); title('Laser Image');
subplot (3,2,3); imshow(Bg); title('Background Image');
subplot (3,2,5); imshow(Dg); title('Difference Image');
subplot (3,2,2); imhist(Lg); title('Laser Image (Histogram)');
subplot (3,2,4); imhist(Bg); title('Background Image (Histogram)');
subplot (3,2,6); imhist(Dg); title('Difference Image (Histogram)');

Dd = double(Dg);
D_min = min(Dd(:));
D_max = max(Dd(:));

J = 255*(Dd - D_min)/(D_max - D_min); J = uint8(J);

figure (2)
subplot (2,2,1); imshow(Dg); title('Laser Image');
subplot (2,2,2); imhist(Dg); title('Laser Image (Histogram)');
subplot (2,2,3); imshow(J); title('Contrast Stretched Image');
subplot (2,2,4); imhist(J); title('Contrast Stretched (Histogram)');

figure (3)
hgram = [0:.1:1];
J1 = histeq(Dg);
subplot (2,2,1); imshow(Dg); title('Laser Image');
subplot (2,2,2); imhist(Dg); title('Laser Image (Histogram)');
subplot (2,2,3); imshow(J1); title('Histogram Equalization');
subplot (2,2,4); imhist(J1); title('Histogram Equalization
(Histogram)');

figure (4)
J3 = imadjust(Dg,[0 0.3], [0 1]);
subplot (2,2,1); imshow(Dg); title('Laser Image');
subplot (2,2,2); imhist(Dg); title('Laser Image (Histogram)');
subplot (2,2,3); imshow(J3); title('Image Adjust');
subplot (2,2,4); imhist(J3); title('Image Adjust (Histogram)');
```

Spatial Filtering

```
L = imread('test0001.bmp');
Lg = rgb2gray(L);

B = imread('test0004.bmp');
Bg = rgb2gray(B);

Dg = Lg - Bg;
Dg = imadjust(Dg,[0 0.3], [0 1]);

% Averaging filter
h = fspecial('average',[3 3]);
A1 = imfilter(Dg,h);

figure (1)
subplot (1,2,1); imshow(Dg) % Original
title('Original Image');
subplot (1,2,2); imhist(Dg)
title('Histogram of Original Image');

figure (2)
subplot (1,2,1); imshow(A1) % Original
title('Image After Average Filtering');
subplot (1,2,2); imhist(A1)
title('Histogram of Image After Average Filtering');

% Median filter
A2 = medfilt2(Dg, [3 3]);

figure (3)
subplot (1,2,1); imshow(A2)
title('Image After Median Filtering');
subplot (1,2,2); imhist(A2)
title('Histogram of Image After Median Filtering');

% Wiener filter
[A3,noise]=wiener2(Dg, [3 3]);

figure (4)
subplot (1,2,1); imshow(A3)
title('Image After Wiener Filtering');
subplot (1,2,2); imhist(A3)
title('Histogram of Image After Wiener Filtering');
```

LIST OF REFERENCES

[1] W. L. Chan., J. Deibel, and D. M. Mittleman, "Imaging with terahertz radiation," *Reports on Progress in Physics*, vol. 70, pp. 1325–1379, July 2007.

[2] P. Shumyatsky and R. R. Alfano, "Terahertz sources," *J. of Biomedical Optics*, vol. 16(3), pp. 033001-1–033001-9, March 2011.

[3] J. Faist, F. Capasso, D. L. Sivco, C. Sirtori, A. L. Hutchison, and A. Y. Cho, "Quantum cascade laser," *Science*, vol. 264, pp. 553–556, April 1994.

[4] M. Tonouchi, "Cutting edge Terahertz technology," *Nature Photonics*, vol. 1, pp. 97–105, February 2007.

[5] B. B. Hu, and M.C. Nuss, "Imaging with Terahertz waves," *Optics Letters*, vol. 20, no. 16, pp. 1716–1718, August 1995.

[6] D.M. Mittleman, M. Gupta, R. Neelamani, R.G. Baraniuk, J.V. Rudd, and M. Koch, "Recent advances in Terahertz imaging," *Applied Physics B*, vol. 68, pp. 1085–1094, April 1999.

[7] D.M. Mittleman, S. Hunsche, L. Boivin, and M.C. Nuss, "T-ray tomography," *Optics Letters*, vol. 22, no. 12, pp. 904–906, June 1997.

[8] A. W. M. Lee, and Q. Hu, "Real-time, continuous-wave Terahertz imaging using a microbolometer focal-plane array," *Optics Letters*, vol. 30, no. 19, pp. 2563–2565, October 2005.

[9] A. W. M. Lee, B. S. Williams, S. Kumar, Q. Hu, and J. L. Reno, "Real-time imaging using a 4.3-THz quantum cascade laser and a 320 x 240 microbolometer focal-plane array," *IEEE Photonics Technology Letters*, vol. 18, no. 13, pp. 1415–1417, July 2006.

[10] A. W. M. Lee, Q. Qin, S. Kumar, B. S. Williams, Q Hu, and J. L. Reno, "Real-time Terahertz imaging over a standoff distance (> 25 meters)," *Applied Physics Letters*, vol. 89, no. 14, pp. 141125-1–141125-3, October 2006.

[11] B. N. Behnken, "Real-time Terahertz imaging using a quantum cascade laser and uncooled microbolometer focal place array," *Ph.D. Dissertation, Naval Postgraduate School*, March 2008.

[12] B. N. Behnken, G. Karunasiri, D. R. Chamberlin, P. R. Robrish, and J. Faist, "Real-time imaging using a 2.8THz quantum cascade laser and uncooled infrared microbolometer camera," *Optics Letters*, vol. 33, no. 5, pp. 440–442, March 2008.

[13] B. N. Behnken, G. Karunasiri, D. R. Chamberlin, P. R. Robrish, and J. Faist, "Optimization of a 3.6-THz quantum cascade laser for real-time imaging with a microbolometer focal plane array," *Proc. SPIE*, vol. 6893, pp. 68930L-1 – 68930L-9, January 2008.

[14] B. S. Williams, "Terahertz quantum-cascade lasers," *Nature Photonics*, vol. 1, pp. 517-525, September 2007.

[15] B. S. Williams, S. Kumar, Q. Hu and J. L. Reno, "High-power terahertz quantum-cascade lasers," *Electron Letters*, vol. 42, no. 2, pp. 89-90, January 2006.

[16] E. R. Mueller, "Terahertz radiation: Applications and sources," *The Industrial Physicist*, pp. 27–29, August/September 2003.

[17] P. H. Siegel, "Terahertz technology," *IEEE Trans. on Microwave Theory and Techniques*, vol. 50, no. 3, pp. 910–928, March 2002.

[18] A.J.L. Adam, I. Kasalynas, J.N. Hovenier, T.O. Klaassen, J.R. Gao, E.E. Orlova, B.S. Williams, S. Kumar, Q. Hu, and J.L. Reno, "Beam patterns of terahertz quantum cascade lasers with subwavelength cavity dimensions," *Appl. Phys. Lett.*, vol. 88, pp. 151105-1–151105-3, April 2006.

[19] E.E. Orlova, J.N. Hovenier, T.O. Klaassen, I. Kasalynas, A.J.L. Adam, J.R. Gao, T.M. Klapwijk, B.S. Williams, S. Kumar, Q. Hu, and J.L. Reno, "Antenna model for wire lasers," *Phys. Rev. Lett.*, vol. 96, pp. 173904-1–173904-4, May 2006.

INITIAL DISTRIBUTION LIST

1. Defense Technical Information Center
   Ft. Belvoir, Virginia

2. Dudley Knox Library
   Naval Postgraduate School
   Monterey, California

3. Professor Dan C, Boger, Code SM/Bo
   Department of Information Systems
   Naval Postgraduate School
   Monterey, California

4. Professor Gamani Karunasiri, Code PH/Kg
   Department of Physics
   Naval Postgraduate School
   Monterey, California

5. Professor David C. Jenn, Code EC/Jd
   Department of Electrical and Computer Engineering
   Naval Postgraduate School
   Monterey, California

6. Mr. Ho Wei Ling
   Electronics Research Laboratory
   DSO National Laboratories
   Republic of Singapore

7. Mr. Ng Mun Wai Raymond
   Electronics Research Laboratory
   DSO National Laboratories
   Republic of Singapore